

Department of the Environment, Transport, Energy and Communications

Swiss Federal Office of Energy SFOE

FINAL REPORT - December 19, 2011

# Experimental and Numerical Investigations on Thermal Energy Storages

Indirect Charging via Immersed Coil Heat Exchangers



#### Client:

Bundesamt für Energie Forschungsprogramme Solarwärme CH-3003 Bern http://www.bfe.admin.ch

Division manager: Jean-Christophe HARDORN Program manager: Andreas ECKMANNS Contract/Project number: 102958 / 153801

#### Contractor:

Institut für Solartechnik SPF HSR Hochschule für Technik Rapperswil Oberseestr. 10 CH-8640 Rapperswil http://www.solarenergy.ch

#### **Authors:**

William LOGIE, william.logie@solarenergy.ch Dr. Elimar Frank, elimar.frank@solarenergy.ch

Except where otherwise indicated, the authors are solely responsible for the work and conclusions presented.

# Contents

Nomenclature					
1	Introduction				
2	2 Theory 2.1 Overall Heat Transfer Coefficient				
	2.2	Convection Coefficients	5		
3	Inve	estigations	7		
	3.1	Contemporary Situation	7		
	3.2	Market Research	8		
	3.3	Reference System	Ĝ		
	3.4	Single-node Heat Exchanger	G		
	3.5	Multi-node Heat Exchanger	11		
	3.6	Transient System Simulation	13		
		3.6.1 Type 340	13		
		3.6.2 Type 60	16		
	3.7	Calorimetry	19		
3.8 Quantitative Flow Visualisation (QFV)			25		
	3.9	Computational Fluid Dynamics (CFD)	28		
		3.9.1 Two-Dimensional Horizontal Cylinder	28		
		3.9.2 Three-Dimensional Multi-Region Model	29		
		3.9.3 Two-Dimensional Axisymmetric Model	31		
4	Discussion and Conclusions				
$\mathbf{A}$	A Straight Tubing				
В	3 Sideways Tables and Figures				
Ri	hling	ranhy	47		

# Nomenclature

		$\mathbf{U}_1$	nits
Symbol	Quantity	Derived	$\mathbf{Base}$
.l ~	Tube diameter		****
$d$ , $\varnothing$	Tube radius		m
r			m
p	Coil pitch		m
L	Length		m
y	Height		m
$D_{A}$	Diameter		$\frac{\mathrm{m}}{2}$
A	Surface or cross-sectional area		$\frac{m^2}{3}$
V	Volume		${ m m}^{3}$
g	Gravity		$m.s^{-2}$
ho	Density	D	$kg.m^{-3}$
$\mu$	Dynamic viscosity	Pa.s	$kg.m^{-1}.s^{-1}$
u	Kinematic viscosity		$m^2.s^{-1}$
$\alpha$	Thermal diffusivity		$m^2.s^{-1}$
$\beta$	Volumetric coefficient of thermal expansion		$K^{-1}$
T	Temperature	1	K
Q	Volumetric flow rate	$\ell.\mathrm{h}^{-1}$	$m^3.s^{-1}$
$\dot{m}$	Mass flow rate	1 1	$kg.s^{-1}$
$c_p$	Specific heat at constant pressure	$J.kg^{-1}.K^{-1}$	$m^2.s^{-2}.K^{-1}$
k	Thermal conductivity	$W.m^{-1}.K^{-1}$	$kg.m.s^{-3}.K^{-1}$
H	Heat (enthalpy)	J	$kg.m^2.s^{-2}$
q	Heat transfer rate (power)	W	$kg.m^2.s^{-3}$
q''	Heat flux	$W.m^{-2}$	${ m kg.s^{-3}}$
h	Convection heat transfer coefficient	$W.m^{-2}.K^{-1}$	
U	Overall heat transfer coefficient	$W.m^{-2}.K^{-1}$	
UA	Overall heat transfer area coefficient	$ m W.K^{-1}$	
Re	Reynolds Number	-	
$\Pr$	Prandtl Number	-	
$\operatorname{Gr}$	Grashof Number	-	
Ra	Rayleigh Number	-	
Nu	Nusselt Number	-	

Continues on next page...

### $\dots continued \ from \ previous \ page$

### Subscript Expansion

coll	Solar Collector
ihx	Immersed Heat Exchanger
tes	Thermal Energy Storage
dhw	Domestic Hot Water
aux	Auxiliary Heater
in	Inlet
out	Outlet
i	Inner
o	Outer
w	Wall
f	Fluid
b	Bulk fluid
$\infty$	Quiescent/free fluid
lm	Log Mean
0	Start/reference condition (e.g. $T_0$ )

# Chapter 1

# Introduction

Prediction of fluid-flow processes involving heat transfer can be accessed via two differing paths; experimental investigation and theoretical calculation. The engineering problem presented in this work is governed not only by a desire to optimise the supply of solar heat to a Thermal Energy Store (TES) by means of Immersed coil Heat Exchangers (IHX); the *performance* of an isolated heat exchanger, perhaps reducing its cost of manufacture, or matters of the system performance as a whole (effects of stratification) - but also to understand intimately the overarching physics at play. As clever as the tools of our investigation seem, what is certainly of more importance is the way we interpret results gained from them.

The most reliable information we can obtain is from direct experimentation, however full scale testing at the desired resolution of system parameters, geometrical variations and real conditions is prohibitively expensive and time consuming. The scaling, reduction and separation of tests into isolated operations allow a significant saving on this but our ability to extrapolate from them is limited. Neither is the equipment necessary for experimentation free from error.

A look at a classical heat transfer or fluid mechanics textbook reveals that only a small set of practical problems can be solved in a closed mathematical form, and that even these solutions can present a formidable task. Thus far development in numerical methods has shown great promise in that the *implications* of a mathematical model can be *worked out* for almost any application under ideal or real conditions, at a low cost and high resolution. These *implications*, however, do not necessarily imply reality itself.

A review of literature reveals a plethora of dissertations, articles and proceedings significant to the common understanding, modelling and conception of our problem at hand. The findings contained in these works have had a large influence on the direction this work has taken; in particular, observations made, whether in theory, numerical modelling or experiments, served as a basis to be built upon.

As early as 1989 [15] it was shown that an optimal exergetic utilisation of incoming energy requires as high an overall heat transfer coefficient (U-value) as possible and a generous charging time period (two hours) for a given mass-flow. The simple reason behind this being that the exergetic efficiency is inverse proportional to the mass-flow; the lower the flow, the higher the efficiency and longer the filling time. The dissertation from Messerschmid [27] took up this criteria and, seeking to optimise the geometric parameters of an IHX with mass-flows of 1000–2000  $\ell$ .h<sup>-1</sup>, found that the most important parameter is that of the relationship from coil-helix-pitch to tube diameter, and that the distance between tube helices should be about the same as the diameter of the tube. Other works exhibit similar findings [1, 41, 33] without specifying what an optimum might be.

Along a path of investigation where the operating conditions reflect the charging stores with solar thermal heat, the phenomena of stratification (first published 1979 [40]) has come to be

known as a criteria of at least, when not more importance [36]. Significant efforts have been made in defining criteria that capture differing degrees of stratification efficiency [16] and evidence for optimising immersed coil heat exchangers under stratified and low collector flow conditions can also be found [39].

However, experiments in the past and also in the investigations presented here have shown that stratification is hard to achieve when charging with an IHX. Thus the questions connected in the topic of optimising the charge of a TES by means of an IHX are manifold:

- can the *heat exchanger efficiency* be improved significantly by changing its geometrical parameters (while keeping the same costs),
- can the *storage stratification* be improved significantly by changing the geometrical parameters of the IHX,
- can the *system efficiency* be improved significantly by changing the geometrical parameters of the IHX,
- can the layout of an IHX be improved for solar thermal systems in order to optimise the combination of costs and system efficiency?

Paradoxically these questions do not necessarily overlap, nor even guide the optimisation process in the same direction. The physical understanding of each component described independently through measurement and the effect of their combination in a system with ancillary components is complex and hard to generalise.

From a simple heat transfer formulation in Section 2 to detailed experimentation in Section 3.7 and numerical studies utilising established Computational Fluid Dynamics (CFD) software in Section 3.9, this report seeks to commiserate the knowledge from both paths of inquisition in a systematic and holistic approach.

# Chapter 2

# Theory

Defining the rate of heat transfer where natural convection is involved requires a transient appreciation of the system in question. Depending on the temperature difference between a given surface and its surrounding fluid, the case of pure conduction is improved by a buoyant flow (gravity dependent) along or away from the surface, steepening the temperature gradient at the surface and therewith increasing the heat flux across it. Figure 2.1 is a schematic representing a TES where an IHX is brought into the bottom of the tank for indirect connection to a solar thermal collector. The problem can be discretised as shown by breaking the IHX into partial sections.

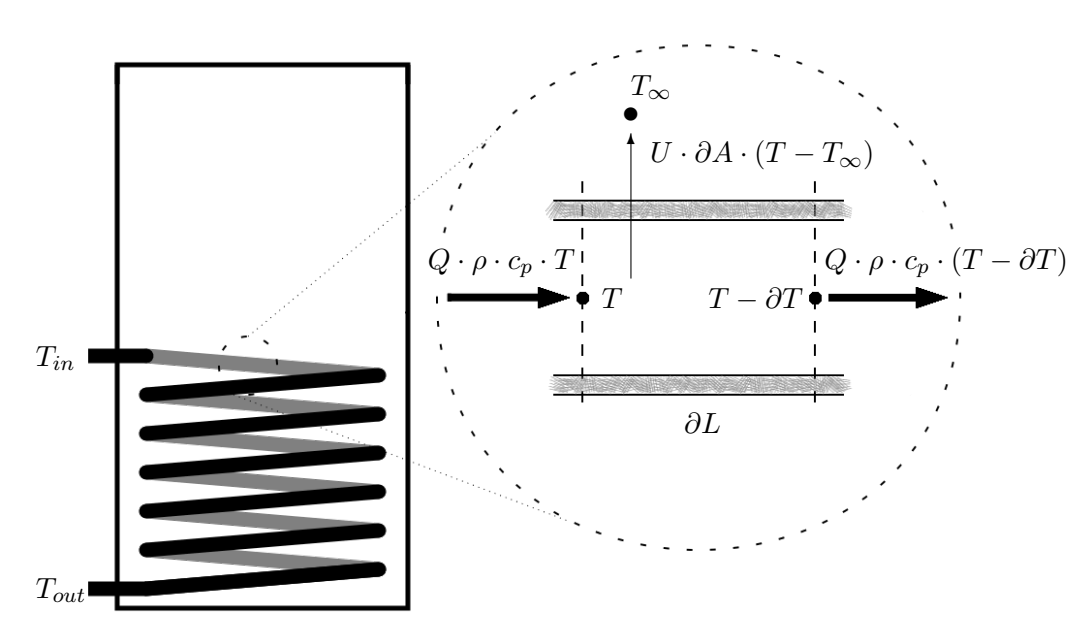


**Figure 2.1:** Illustration of a TES with an IHX showing an exploded view of a discrete IHX section with tube length  $\partial L$  and surface area  $\partial A$ .

The heat flow for the exploded section illustrated can be expressed in Equation 2.1 and simplified to Equation 2.2. Both  $c_p$  and  $\rho$  can be evaluated as functions of respective fluid temperatures (and concentration, in the case of ethylene or propylene glycol), so long as implementation doesn't infringe upon the conservation of mass through the system.

$$Q \rho c_p T = U \partial A_o (T - T_\infty) + Q \rho c_p (T - \partial T)$$
(2.1)

$$\frac{U\,\partial A_o}{Q\,\rho\,c_p} = \frac{\partial T}{T - T_\infty} \tag{2.2}$$

Indexing the variables and integrating over the length of the IHX develops the problem to Equation 2.3.

$$\int_0^{A_o} \frac{U_j \,\partial A_o}{Q \,\rho_j \,c_{p_j}} = \int_{T_{in}}^{T_{out}} \frac{\partial T}{T_j - T_{\infty_j}} \tag{2.3}$$

#### 2.1 Overall Heat Transfer Coefficient

The determination of the heat transfer coefficient U requires a modelling of the combined conduction and convection through the IHX tubing. We begin by looking at the resistive equation for the heat exchanger wall and build on this with the convective and fouling factors on either side. For a tube wall with inner radius  $r_i$  and outer radius  $r_o$  the conductive resistance equation takes the form:

$$R_w = \frac{\ln\left(\frac{r_o}{r_i}\right)}{2\pi k_w \partial L},\tag{2.4}$$

for a discrete section of the IHX with length  $\partial L$ .

Adding now the coefficients of convection h for inner and outer fluids, fouling factors<sup>1</sup>  $R''_f$  and the enhancement of heat transfer through the increasing of inner or outer surface efficiencies<sup>2</sup>  $\eta$ , the outer heat transfer coefficient for any IHX section  $U_j$  can be calculated given knowledge of the variables as related in Equation 2.5.

$$(U_j \partial A_o)^{-1} = \frac{1}{\eta_i h_{i_j} 2\pi r_i \partial L} + \frac{R''_{f,i}}{\eta_i 2\pi r_i \partial L} + R_w + \frac{R''_{f,o}}{\eta_o 2\pi r_o \partial L} + \frac{1}{\eta_o h_{o_j} 2\pi r_o \partial L}$$
(2.5)

Similar to a model used for flat-plate collectors [12, 3] and terminal heat exchangers [4], a mathematical formulation of an IHX viewed as a one-dimensional sink was implemented. Neglecting things like fouling and fin factors to begin with, the efficiency of an IHX is defined as the ratio of actual useful heat transferred to the optimum which would result if the IHX outer surface were at the local bulk fluid temperature:

$$F'_{j} = \frac{\frac{1}{h_{o_{j}}}}{\frac{r_{o}}{r_{i}} \frac{1}{h_{i_{j}}} + \frac{r_{o}}{k_{w}} \ln\left(\frac{r_{o}}{r_{i}}\right) + \frac{1}{h_{o_{j}}}}.$$
(2.6)

Utilising log mean temperature analysis for each partial length of IHX in question, the outlet temperature can be found using:

$$T_{out_j} = T_{\infty_j} + (T_{in_j} - T_{\infty_j}) \exp \frac{-h_{o_j} \partial A_o F_j'}{\dot{m} c_n}, \tag{2.7}$$

and the *useful* rate of heat transfer can be found as is customary:

$$q_j = \dot{m} c_p \left( T_{out_j} - T_{in_j} \right). \tag{2.8}$$

Using the IHX rejuvenation factor  $F_R$  (a.k.a. removal factor for flat-plate collectors) and flow factor F'':

$$F_{R_j} = \frac{q_j}{\partial A_o h_{o_j} (T_{\infty_j} - T_{in_j})} \tag{2.9}$$

$$F_j'' = \frac{F_{R_j}}{F_j'},\tag{2.10}$$

<sup>&</sup>lt;sup>1</sup>e.g. rust and lime deposits can be treated by introducing an additional thermal resistance.

<sup>&</sup>lt;sup>2</sup>e.g. Section 3.6 pp. 137–155 and Section 8.2 pp. 521–524 [20]

the average temperature of the wall  $\overline{T}_w$  and bulk fluid inside the IHX  $\overline{T}_b$  can be found using:

$$\overline{T}_{w_j} = T_{in_j} + \frac{q_j}{\partial A_o} \frac{1 - F_{R_j}}{h_{o_j} F_{R_j}}$$
(2.11)

$$\overline{T}_{b_j} = T_{in_j} + \frac{q_j}{\partial A_o} \frac{1 - F_j''}{h_{o_i} F_{R_i}}.$$
(2.12)

Depending on what the unknowns in Equations 2.6 to 2.12 are, an iterative approach can account for non-linearity (e.g. temperature dependent variables); following a first approximation for  $\overline{T}_b$  (e.g.  $\frac{T_{in}+T_{out}}{2}$ ) and a determination of  $h_i$  from [14]; either  $\overline{T}_{w_j}$  is known from measurements and an iteration seeks values for  $h_{o_j}$  or this is determined from correlations [7, 28].

On the assumption that the storage temperature  $T_{\infty}$  and the heat transfer coefficient U are constant over the total length of the IHX, Equations 2.6 to 2.12 can be solved for the complete IHX area  $A_o$ .

#### 2.2 Convection Coefficients

Whether we determine convection coefficients by way of correlation, based on measurements or computationally, it is worth our while to review their derivation here. In Figure 2.2 we see the cross section of a horizontal tube with which we can visualise the information relevant in the determination of convection coefficients h and therewith the Nusselt numbers Nu.

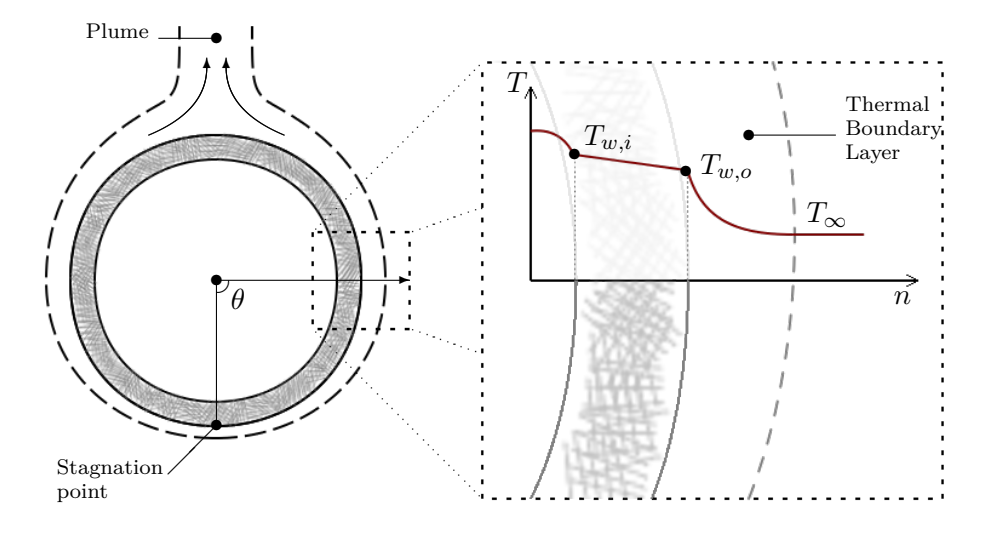


**Figure 2.2:** Illustration of horizontal tube cross section showing development of convective thermal boundary layer given the presence of heat exchange from the internal to the external fluid.

The wall heat flux of any point is found by way of the temperature gradient normal to its surface (Equation 2.13), from which the convection coefficient can be calculated as in Equation 2.14.

$$q'' = k_f \frac{\partial T}{\partial n} \Big|_{n_w} \tag{2.13}$$

$$h = \frac{q''}{T_w - T_\infty} \tag{2.14}$$

For more universal comparison the boundary layer equations are normalised for the characteristic length of relevance (e.g. outer tube diameter  $d_o$ ) and absolute temperatures, for which

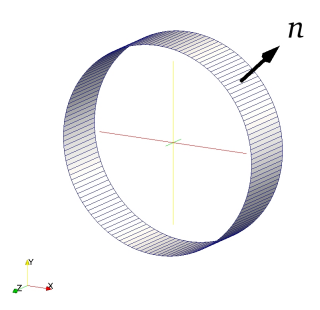


**Figure 2.3:** An example of n on the discretised external surface area of a cylindrical tube

the dimensionless independent variables for the distance normal to surface and temperature are required;

$$n^* = \frac{n}{d_o} \tag{2.15}$$

$$n^* = \frac{n}{d_o}$$

$$T^* = \frac{T - T_\infty}{T_w - T_\infty}.$$

$$(2.15)$$

As such the expression for the convection coefficient becomes that of Equation 2.17.

$$h = +\frac{k_f}{d_o} \frac{\partial T^*}{\partial n^*} \bigg|_{n_{w,o}} \tag{2.17}$$

From this the Nusselt Number can be defined as in Equation 2.19 and is equivalent to the dimensionless temperature gradient at the surface, providing us with a measure for the increase in wall heat flux due to convection.

$$Nu_{d_o} = \frac{h d_o}{k_f} \tag{2.18}$$

$$= + \frac{\partial T^*}{\partial n^*} \bigg|_{n_{w,o}} \tag{2.19}$$

It follows from Equation 2.19 and Figure 2.2 that for cylindrical geometry the Nusselt Number becomes a function of the angular coordinate around the tube  $\theta$  and the fluid properties as expressed with the *Reynolds* and *Prandtl* Numbers;

$$Nu_{d_0} = f(\theta, Re_{d_0}, Pr). \tag{2.20}$$

Typically, as in the case of free convection from horizontal cylinders [7, 28] or forced convection inside coiled tubes [14], correlations for the overall Nusselt Number have been determined from a plethora of experiments which brings about the more common awareness of the Nusselt Number as being an average over the relevant circumference;

$$\overline{\mathrm{Nu}}_{d_o} = \frac{1}{2\pi} \int_0^{2\pi} + \frac{\partial T^*}{\partial n^*} \bigg|_{n_{w,o}} \mathrm{d}\theta. \tag{2.21}$$

# Chapter 3

# Investigations

In the passing of this project eight heat exchangers differing within the representative market range were identified and provided for testing by companies from Austria, Germany, Holland and Switzerland (see Table B.1). Before getting into their calorimetry measurements, it is worth our while to understand the general behaviour of immersed coil heat exchangers from a systematic perspective and within the current market situation.

#### 3.1 Contemporary Situation

current TES systems where simple solar

integration is envisaged at point of storage

manufacture.

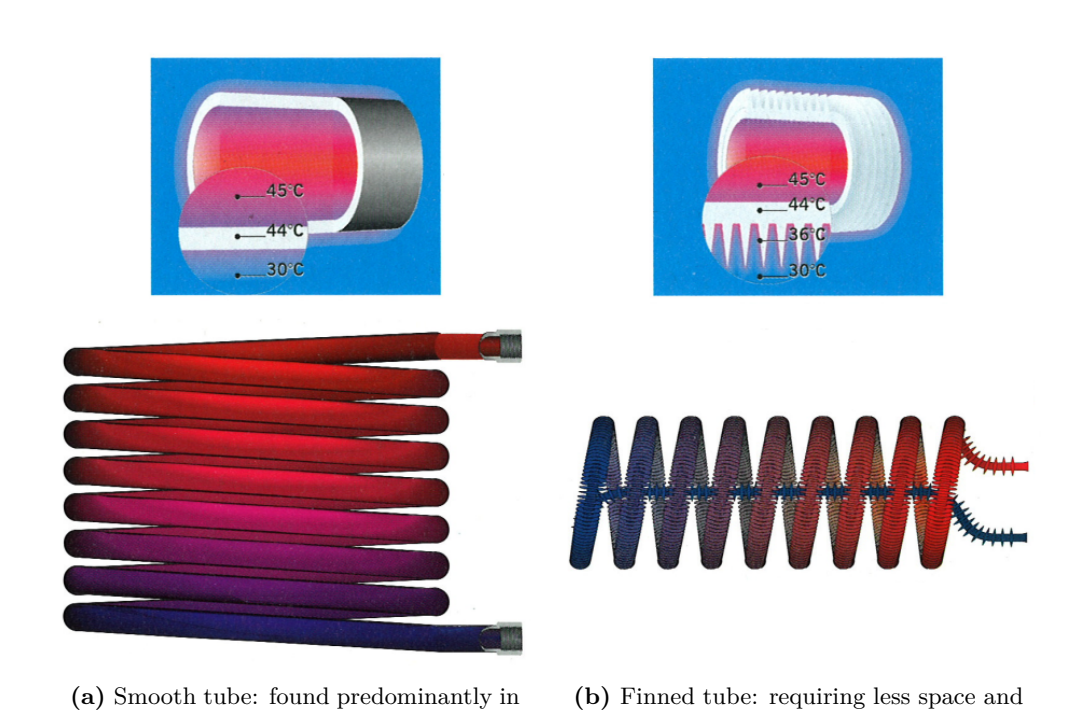


**Figure 3.1:** Typical immersed coil heat exchangers (pp. 4–56 [8]). The operating temperatures seem to illustrate a high heat flux, although no information about volumetric flow is given.

IHX surface area, this more traditional

IHX design can be retrofitted through a

As identified in Figure 3.1, taken from the Deutsche Gesellschaft für Sonnenenergie (DGS) handbook on solar thermal systems, we are typically talking about variations of the helical coiled

variety; the simplest of which (Figure 3.1a) can be improved on by the use of fins (Figure 3.1b) or corrugations to increase surface efficiencies and reduce susceptibility to calcification. The DGS goes on to say that one should optimally allow for  $0.25~\mathrm{m}^2$  smooth heat exchanger surface for every square meter of collector, respectively  $0.35~\mathrm{m}^2$  finned heat exchanger. The handbook [2] from the Swiss Federal Office of Energy (SFOE) elaborates a little more on this with a range for both smooth  $(0.15-0.25~\mathrm{m}^2)$  and finned  $(0.25-0.35~\mathrm{m}^2)$  and mentions the conditions under which these are valid; namely a maximum specific collector power of 700 W.m<sup>-2</sup> achieving a temperature difference of  $10-15~\mathrm{K}.^3$ 

#### 3.2 Market Research

Indeed, when one takes a look at current trends, as for example is illustrated in Figure 3.2, the market seems to follow - or perhaps the recommendations are derived from its best-practises. For lack of intimate knowledge concerning the source of these recommendations, it was assumed that they are based on a combination of theory and experience and have more or less validated themselves with time. The spread of the data collected implies that there are primary variables in

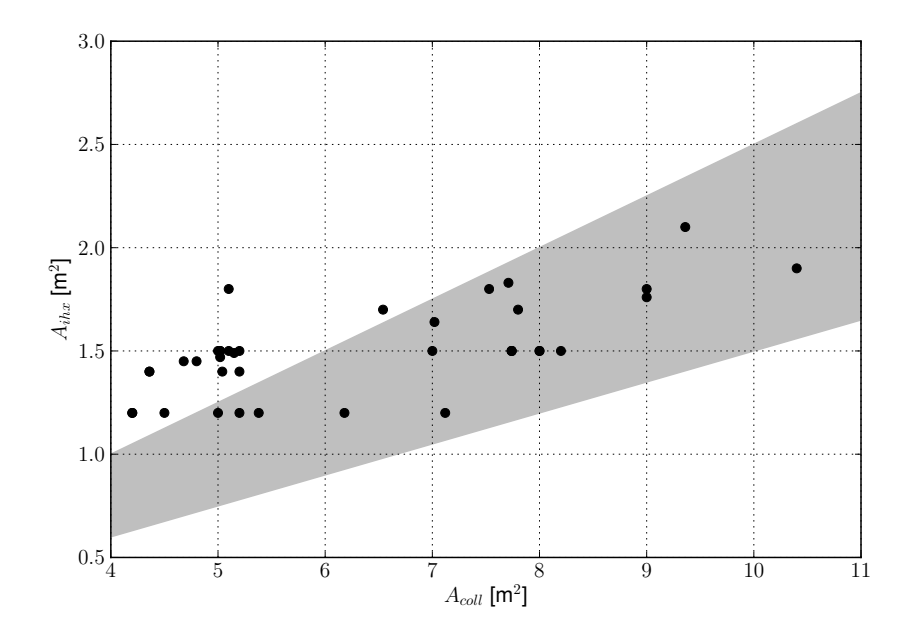


**Figure 3.2:** A sample of 38 solar DHW packages available on the German speaking market [23] showing the relationship of solar collector area to IHX surface area. The *grey* area represents the range recommended by DGS and SFOE handbooks for dimensioning IHX in relation to collector area.

the design of a SDHW system that influence how much area and volume a solar IHX receives. A Thermal Energy Storage (TES) of specific volume, requiring to fit through a standard basement door, fitted with enough insulation and the desired auxiliary heater etc.— receives a solar IHX area relating to either collector area or storage volume (or both). Predominately between  $^3/_4$ " and  $1^1/_2$ " tubing is used and the length of tubing is coiled with a pitch approximately  $^1/_3$  the

<sup>&</sup>lt;sup>1</sup>German: Wellrohr.

<sup>&</sup>lt;sup>2</sup>This has been claimed by several manufacturers but, as far as the authors know, not been proven yet with systematic and reproducible measurements.

<sup>&</sup>lt;sup>3</sup>No further supporting information is given; e.g. volumetric flow rate.

diameter of the tubing, from the inlet (coming from the collector) to the outlet at the bottom of the tank. Sometimes obstacles along the way need to be avoided or accommodated for, for example when a flange for cleaning or retrofitting auxiliary heat is conceived on the side of the TES, or maybe some *dead-zone* at the bottom of the tank needs to be reached. In such instances one can see larger pitches and off-axis coil sections.<sup>4</sup>

#### 3.3 Reference System

From a look at the market an illustrative reference system was defined from a statistical average of systems with a tank volume between 300 and  $550\ell$ , around which experimentation and modelling could be oriented (Table 3.1). The system does not excel in any way - in fact the generic collector, control strategy, insulation quality and auxiliary heater used are of average quality - herewith we stress the desire to see what the operating conditions of a typical system is. The conditions under which the IHX operates required the defining of ancillaries and control strategies more detailed in Figure B.1. The reader may wonder why a variable collector and

 $\mathrm{m}^{\overline{2}}$ Flat plate collector area 5 - 7Collector inclination 45 200  $\ell.d^{-1}$ DHW consumption  $^{\circ}C$ DHW delivery temperature 45 TES Volume 400 TES Height 1500 mm100 Insulation thickness mmTES operating fluid Water Solar IHX area 1.4 - 1.7 $V_{PG}.V^{-1}$ Solar IHX operating fluid 33% Propylene-glycol  $\mathrm{m}^2$ 1.2 Auxiliary IHX area Auxiliary IHX operating fluid Water

Table 3.1: SDHW Reference System

IHX area is itemised, which another look at Figure 3.2 can shed light on. It seems that in this range of storage and collector sizes the solar IHX area is quite well endowed and that the deviation is more dependent on manufacturers than what the handbooks recommend. Seeing as a higher area of average collector harvests similar heat to a smaller area of good collector (maybe combined with better sensor positions and control settings), the exactness of these numbers can be interpreted at the readers discretion.

### 3.4 Single-node Heat Exchanger

Taking this reference system we consider how one might go about modelling it. The simplest storage model we can imagine is an isotropic one. For theoretical experiments this case serves as a pleasant reference point, from which all real stratified cases deviate for the better.

Reviewing the theory laid out in Section 2, we are reminded that the manner by which heat is transferred is dependent above all on mass-flow and the temperature difference between delivery and the TES. Intuitively we are aware that if the mass-flow through the heat exchanger is high enough we can induce turbulence inside the tube and therewith increase heat transfer. Alternatively we can reduce the mass-flow and rely on a high  $\Delta T$  between the IHX and TES to

<sup>&</sup>lt;sup>4</sup>Further reading: [23].

transfer heat. In any case, we'd like to be able to see how variation in geometry parameters (i.e. IHX tube diameters, lengths and areas) respond to the range of mass-flows and temperature differences relevant for SDHW operation.

To this purpose we implement the model laid out in Section 2 in a similar way to TRNSYS Type 60 (see Section 3.6.2) but with the correlations from Gnielinski [14] for forced convection and pressure drop in helical coils, and Churchill and Chu [7] or Morgan [28] for free convection from horizontal cylinders. Varying the volumetric flow for a fixed inlet temperature in the example of IHX C shown in Figure 3.3 we can try to find the operating conditions eluded to in the IHX design recommendations of the SFOE handbook (Section 3.1). For comparison, Figure A.1

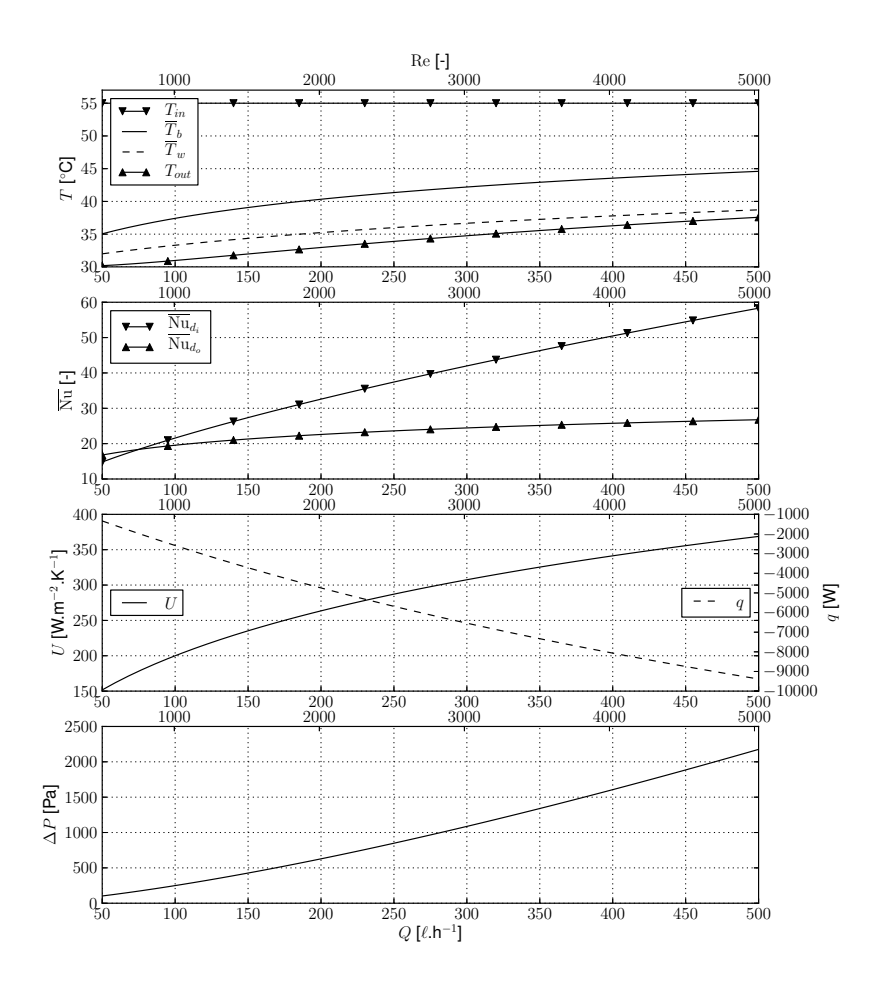


**Figure 3.3:** Modelled performance of IHX C (see Table B.1) with 33 % propylene glycol for a varying volumetric flow rate (Reynolds Number) given a constant inlet temperature of 55  $^{\circ}$ C and an isotropic storage tank at 30  $^{\circ}$ C.

shows the same IHX as modelled with water and an inner correlation for straight tubing. There are three things that spring to our attention in Figure 3.3; Reynolds (Re) numbers are lower (viscosity of propylene glycol), the expected transition from laminar to turbulent (Re between 2300 and 3000) is not forthcoming and the respective overall internal Nusselt ( $\overline{\text{Nu}}_{d_i}$ ) numbers are up to 20% smaller and increase less in proportion to Re. Alas, we have encountered the so called Dean flow; secondary flow due to centrifugal force (axial acceleration perpendicular to flow direction) improves heat transfer [6], most notably in the laminar region, but also dampens

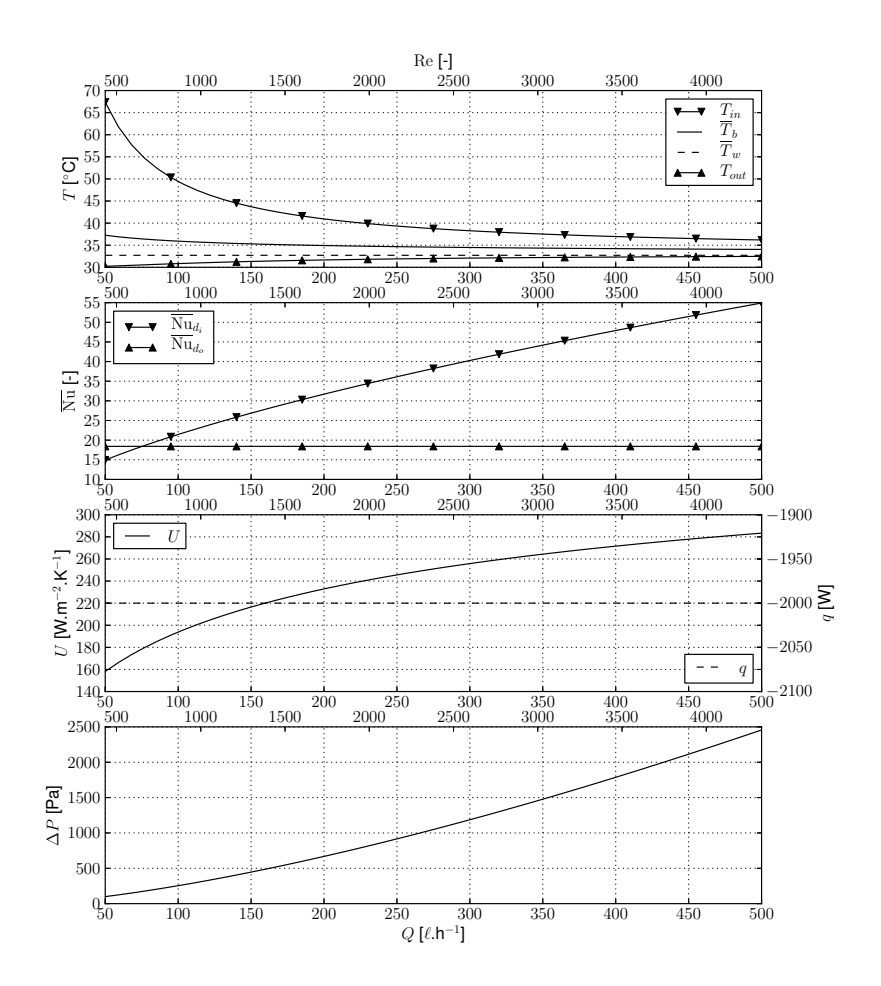


**Figure 3.4:** Performance of IHX C (see Table B.1) for a varying volumetric flow rate (Reynolds Number) given a constant heat transfer of 2000 W and an isotropic storage tank at 30°C.

the onset of turbulence.<sup>5</sup> We can also observe the response of IHX C assuming that it is receiving 2000 W. Taking a look at Figure 3.4, a few more things become apparent. Again the dependency of the overall heat transfer coefficient U on mass flow remains dominant and temperature differences adjust themselves accordingly. What at first seems surprising is that the overall outer Nusselt number  $(\overline{Nu}_{do})$  remains constant with change in volumetric flow. On second glance however this is explained by the nature of our assumptions. We have after all modelled the entire IHX with one node, and as such there is no local resolution of heat transfer. Figure A.2 offers a reference for constant q as did Figure A.1 for constant  $T_{in}$ .

As stipulated in Section 2, we were expecting this, and as such we can develop our modelling to observe not only the local variation in heat transfer along the length of an IHX but also for varying storage temperature.

### 3.5 Multi-node Heat Exchanger

Modelling now the isotropic TES but with the IHX discretised into *sub domains*, we can compare in detail the distribution of heat transfer along the length or height of the IHX. The two constant

<sup>&</sup>lt;sup>5</sup>In fact, transition to turbulence is expected with Re approaching 7400; an equivalent volumetric flow around  $1000 \ \ell.h^{-1}$ 

collector flow strategies widely used are the so called low or high flow principles, referring to specific collector flows of 10-15 or  $\geq 40~\ell.h^{-1}$  per m<sup>2</sup> collector area respectively. For our reference system we would like to see what this difference is and select as such the two flow rates of 70 and  $350~\ell.h^{-1}$  for closer inspection. For the purpose of later modelling we can begin to translate the length of each IHX helix into its respective height such that a relation to TES geometry may be established. We are now ready to observe in Figure 3.5 how the heat transfer varies along the length of IHX C for our chosen volumetric flows. We can see clearly how in the case of

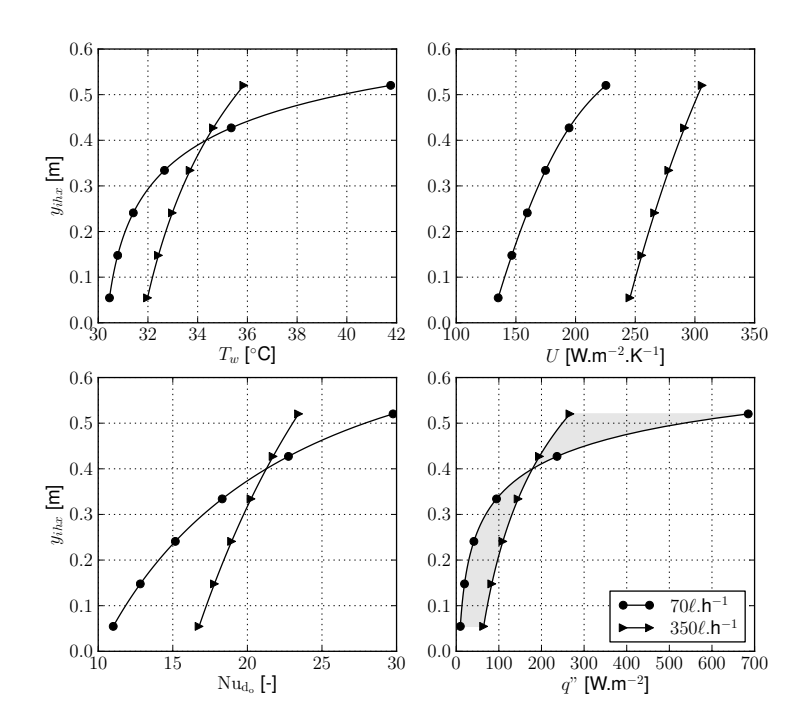


Figure 3.5: Wall temperature  $T_w$  and heat flux q'' of IHX C plotted against the respective helix height within a TES for high and low flow charging of an isotropic TES at 30 °C (note: having ensured a total heat transfer rate of 2000 W in both cases, an integration of the grey area in the lower right plot for q'' should return a zero result).

low-flow there is a greater balance of heat flux entering the TES at the top of the IHX. What we are not capturing however is the effect the buoyant flow from the lower coils have on the upper coils, seeing as the temperature of the fluid inside the buoyant flow is higher than the otherwise surrounding fluid  $(T_{\infty})$  but has an associated *forced convection*. To discern the extent of this effect, we must increase the resolution and complexity of our modelling by a significant factor (Section 3.9) or rely on calorimetry measurements for real data (Section 3.7).

Out of curiosity we can see how the IHX responds to an arbitrarily stratified store in Figure 3.6. What this modelling does not account for is the effect the temperature gradient (stratification) over the height of a single coil tube has on its respective overall Nusselt number. There is one work known to the authors in which this phenomena was studied [13]. Given accurate information about the temperature gradient, this method allows even the prediction of the penetration height of the plume from any single coil. Although not implemented here nor later in the calorimetry measurements, this work could prove most insightful in future transient TES/IHX modelling.

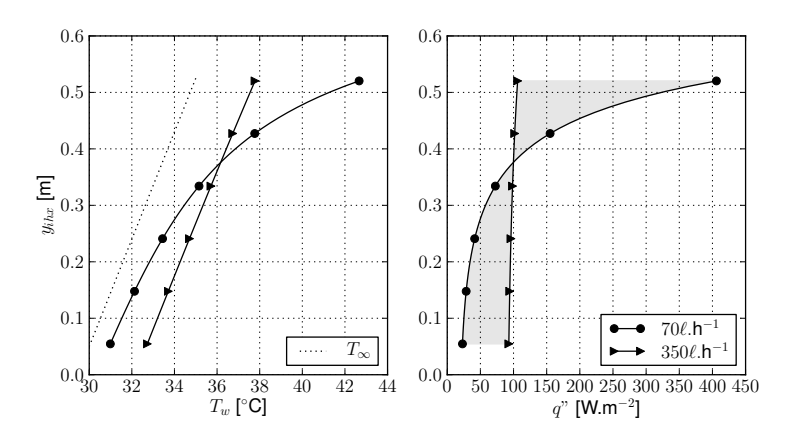


Figure 3.6: Wall temperature  $T_w$  and heat flux q'' of IHX C plotted against the respective helix height within a theoretically stratified TES ( $T_\infty$  varies with height y). Again we have ensured a total heat transfer rate of 2000 W.

#### 3.6 Transient System Simulation

One last digression before we head into the laboratory is a study of annual transient simulations. The intention is to identify statistically significant operating conditions for defining the laboratory protocol— in other words, gather a feel for non-laboratory conditions. For modelling SDHW stores there are two main store stratification models which include the modelling of immersed heat exchangers, each having their advantages depending on the information at hand. The TRNSYS Type 340 (a.k.a MULTIPORT) model [9, 10] was developed alongside the Component Testing - System Simulation (CTSS) method for the testing of stores according to CEN/TS 12977 [5] by way of black-box parameter identification. The other approach is a one-dimensional physical modelling of conduction and convection with TRNSYS Type 60 [21], which is more suited for situations where no measurement data but a clear idea of IHX geometry is available. Either way, stratification is modelled by way of a control volume formulation in which a differential equation for temperature diffusion and entrainment (i.e. no hydrostatic pressure effects) is solved iteratively for each node i in the TES.

#### 3.6.1 Type 340

As described in [9], any TES node i in which the IHX is found, temperature and mass-flow dependency of the overall heat transfer coefficient between the IHX and TES node is handled with the following parametric equation:

$$\frac{UA_{ihx}^*}{n_{ihx}} = \frac{UA_{ihx}}{n_{ihx}} F_{ihx} \dot{m}_{ihx}^{b_1} \left[ T_{in_i} - T_{\infty_i} \right]^{b_2} \left[ \frac{T_{in_i} + T_{\infty_i}}{2} \right]^{b_3}, \tag{3.1}$$

where  $UA_{ihx}$ : Overall heat transfer area coefficient,

 $n_{ihx}$ : Number of nodes in TES occupied by the IHX,

 $F_{ihx}$ : Factor for time dependency,

 $\dot{m}$ : Mass-flow rate through the IHX,

 $T_{in_i}$ : Inlet temperature for IHX in node i,

 $T_{\infty_i}$ : TES temperature in node i,

 $b_1, b_2, b_3$ : Exponents for the dependency of  $UA_{ihx}$  on mass-flow  $(b_1), \Delta T_{ihx,tes}$ 

 $(b_2)$  and things like viscosity  $(b_3)$ .

Significant studies were performed on the reference system defined earlier with Type 340 (see [23]). The most sensible starting point for simulations with Type 340 is to access mea-

surement data or crude calculations that allow some derivation of an overall heat transfer area coefficient UA. As our thoughts developed from Section 3.4 onwards, so too do our requirements for a more universal modelling grow (independent of volumetric flow or temperatures), which we can see was accounted for in the development of Equation 3.1. Such a parametric equation is not very intuitive however, especially when it comes to finding suitable exponents  $b_1$ - $b_3$ , and there is no universally published methodology known to these authors for fitting sets of experimental data to Equation 3.1. Although attempts were made, lack of experience proved a hindrance and as such published values of  $b_1$  and  $b_3$  were used [11]. Adjusting slightly for our reference system, we could thus simulate the varying collector flows chosen in Section 3.5. The question of whether the results are of value was analysed by way of contour plots<sup>6</sup>, the first of which we can see in Figure 3.7

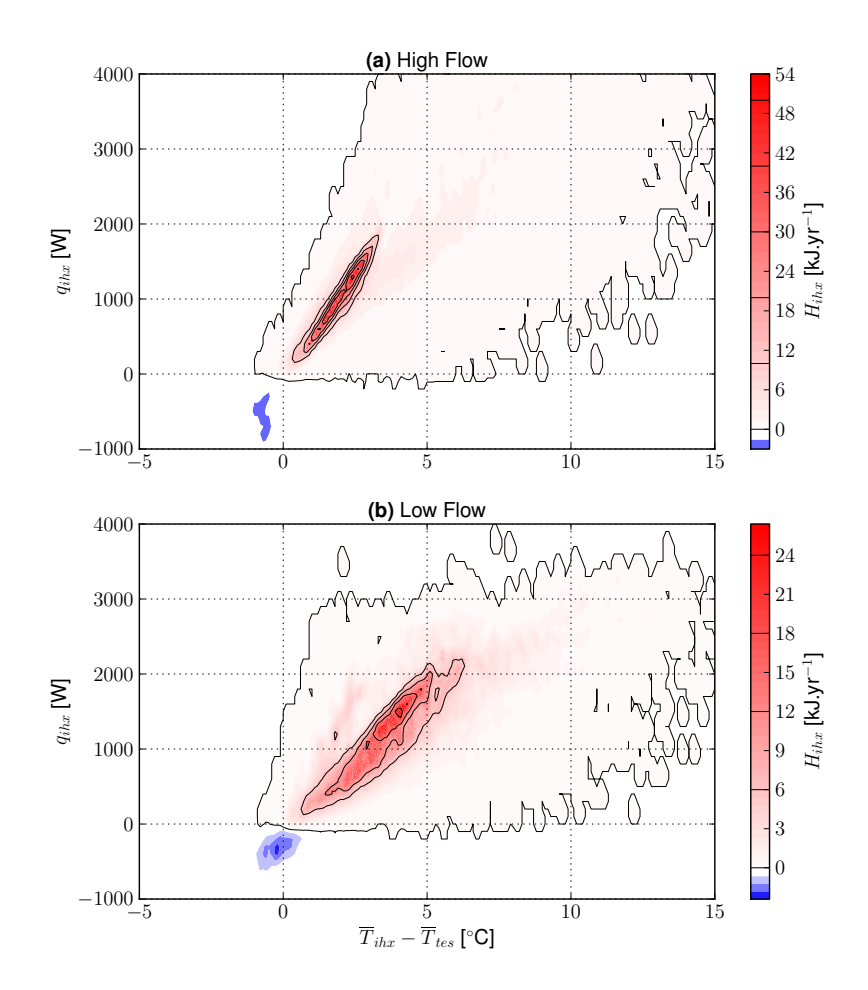


Figure 3.7: Contour plot of a generic IHX power q against the bulk mean temperature difference  $\overline{T}_{ihx} - \overline{T}_{tes}$  as derived from Type 340 outputs. Whereas we would prefer illustrating the log mean temperature difference on the x-axis, Type 340 only offers us the mean IHX temperature as an output, which makes derivation of  $\Delta T_{lm}$  impossible.

<sup>&</sup>lt;sup>6</sup>The visualisation methodology is a style of histogram where discrete bins are spanned over the expected range of operating conditions ( $\Delta T$ , q and U). For each coordinate between any two chosen axes, the amount of energy transferred at that condition is summed over the year of simulation data— therefore the height of the contours depends on the amount of discrete bins.

The first thing we notice is a rather diffuse spread of operating conditions, which to the best of our awareness is a by-product of imperfect TRNSYS implementation. There appear to be many time-steps in the simulation where switching creates problems for the successive iteration algorithm. The advantage of this plot visualisation however is that stable conditions at which large sums of energy are transferred become highlighted (red). In Figure 3.7 we can see that a large portion of energy is transferred at a heat transfer rate below 2000 W, the temperature differences exhibiting the expected high or low flow operation.

In Figure 3.8 we can see how the overall heat transfer coefficient is modified by  $b_1$  and in Figure 3.9 how it is changed according to the mean temperature in both heat exchanger and storage with  $b_3$ <sup>7</sup>. On comparing these *U*-values with those obtained earlier in Section 3.4, we see some level of agreement.

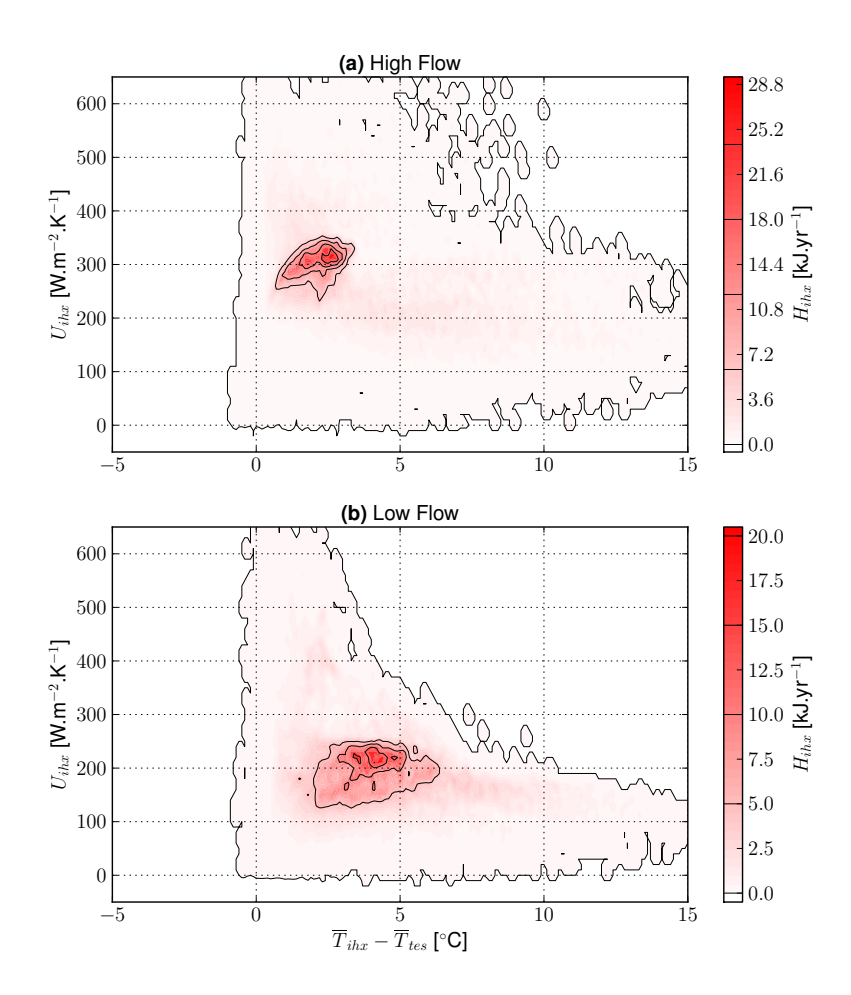


Figure 3.8: Contour plot of a generic IHX overall heat transfer coefficient U against the bulk mean temperature difference  $\overline{T}_{ihx} - \overline{T}_{tes}$  as derived from Type 340 outputs.

 $<sup>^{7}</sup>$ Generally all fluid properties remain constant throughout TRNSYS simulations, therefore any change in U due to the temperature dependent change in viscosity, density or specific heat is modelled with this exponent.

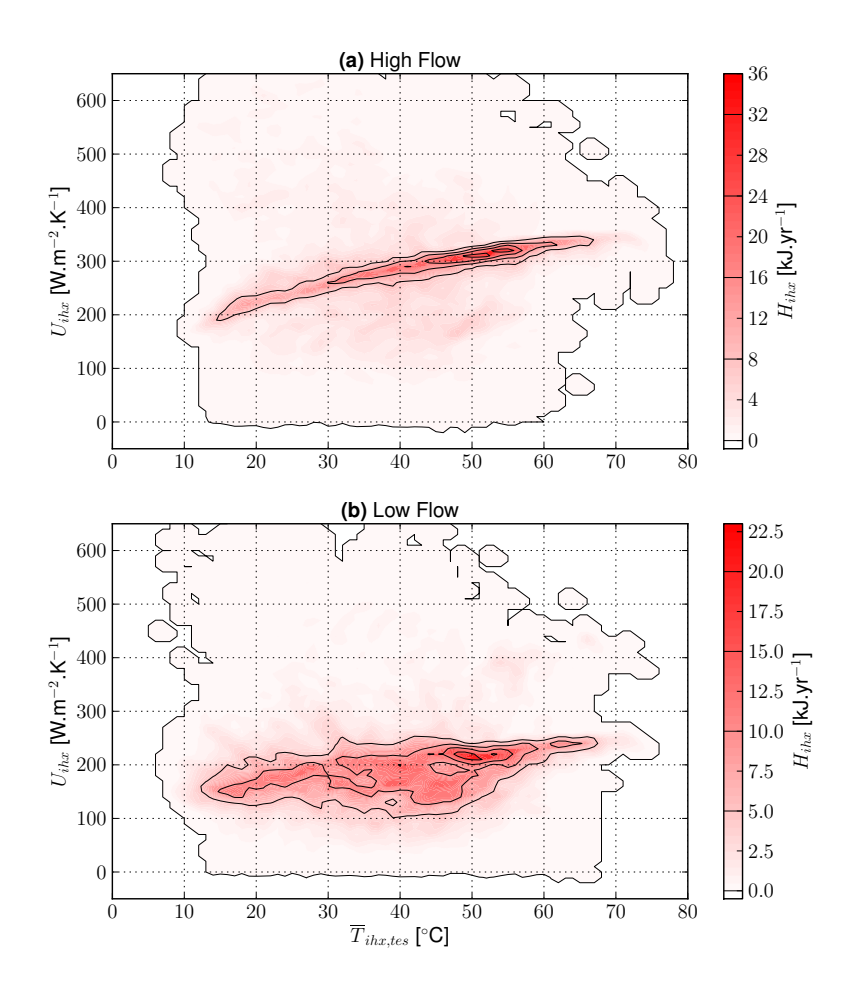


Figure 3.9: Contour plot of a generic IHX overall heat transfer coefficient U against the bulk mean temperature of both IHX and TES  $\overline{T}_{ihx,tes}$  as derived from Type 340 outputs.

#### 3.6.2 Type 60

Descending from the same one-dimensional understanding of radial heat conduction in tubes we've seen in Section 2, the convection occurring on both sides - forced on the inside and combined (forced and free) on the outside - is modelled with correlations derived from experiments on straight horizontal tubing [12, 20]. For any node i in which the IHX is found, Equation 2.5 is solved to find the partial area heat transfer coefficient  $UA_{ihx_i}$  between the respective IHX and TES node. By way of internal functions for calculating the density  $\rho$ , specific heat  $c_p$ , conductivity k and dynamic viscosity  $\mu$  of the operating fluids water and ethylene/propylene glycol<sup>8</sup>, a dynamic similitude approach uses the diameters of the IHX tubing as characteristic lengths.

Simulations with Type 60 led to some interesting results. In Figure 3.10 we can visually extract the relative frequency of IHX power in relation to the log mean temperature difference, both of which are direct outputs from the Type 60. What immediately catches our eye is the fact that volumetric flow doesn't seem very well resolved between the contour plots for high and low flow. Stable operation in both cases seems to transfer heat at more or less the same log mean temperature differences. Looking also at Figure 3.11 we can see the spread of U-values for IHX

 $<sup>^8{\</sup>rm The~concentration~of~ethylene~glycol~is~limited~to~55–85\%}$ 

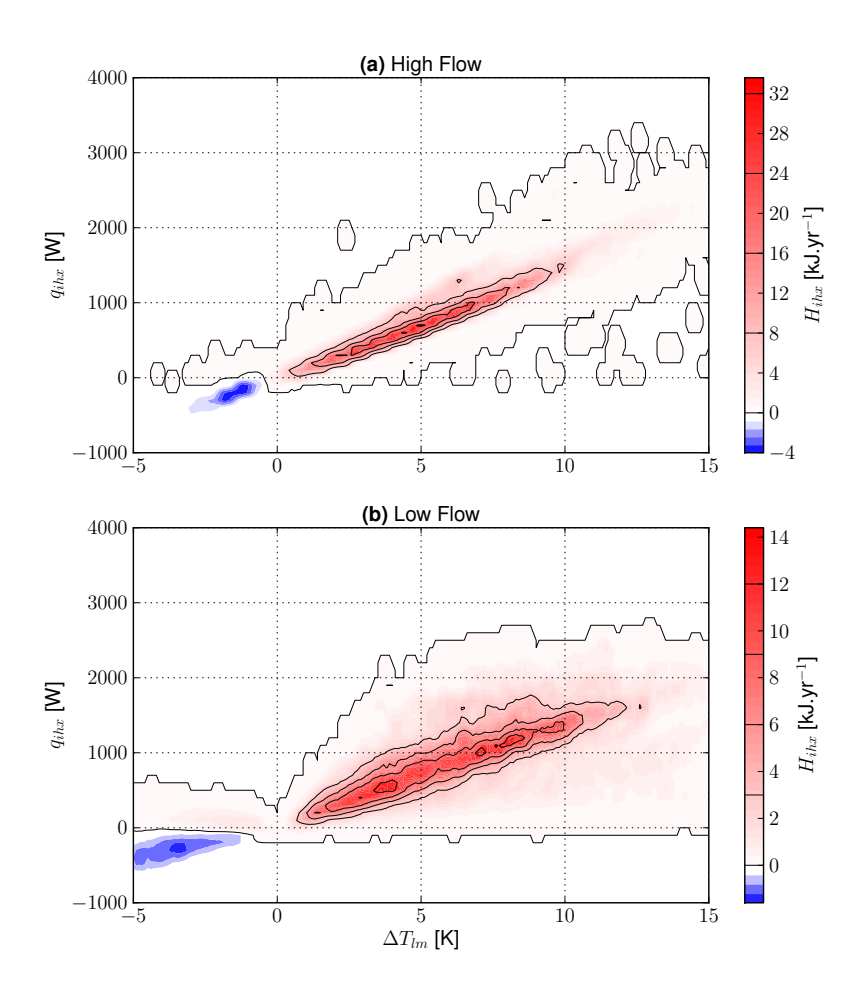


**Figure 3.10:** Contour plot of IHX C power q against the log mean temperature difference  $\Delta T_{lm}$  as output from Type 60 modelling.

C but the comparison we expect is unforthcoming. On closer inspection it seems that Type 60 calculates higher heat transfer coefficients for the low flow case than what we would expect ( $\approx 170~{\rm W.m^{-2}.K^{-1}}$ ). An inquisition into the reason for this was not undertaken, but we can speculate that some lower *cut-off* limit in the modelling of either volumetric flow dependency or Nusselt numbers is responsible for this.<sup>9</sup>

Whether we use Type 340 or Type 60, simulations with TRNSYS imply that low-flow operation leads to mildly better solar fractions (between 1 and 3%— see also [36])<sup>10</sup>, although it need not only be due to the higher delivery of heat into the TES we witnessed in Figures 3.5–3.6. The reader would have noticed the removal of heat (blue contours) and know that this can be reduced - if not completely avoided - with proper selection of the dead-band temperature differences and the temperature sensor position for the collector pump controller. We did not optimise this as our intention was to have a reference system representing something like a standard or average case.

 $<sup>^{9}</sup>$ In other simulations a temperature dependent step-wise artefact was observed in U-values.

<sup>&</sup>lt;sup>10</sup>Balanced at the TES, the annual Solar Fraction is defined as the ratio of heat provided by the collector to the total heat provided to the TES;  $SF = \frac{H_{coll}}{H_{coll} + H_{aux}}$ .

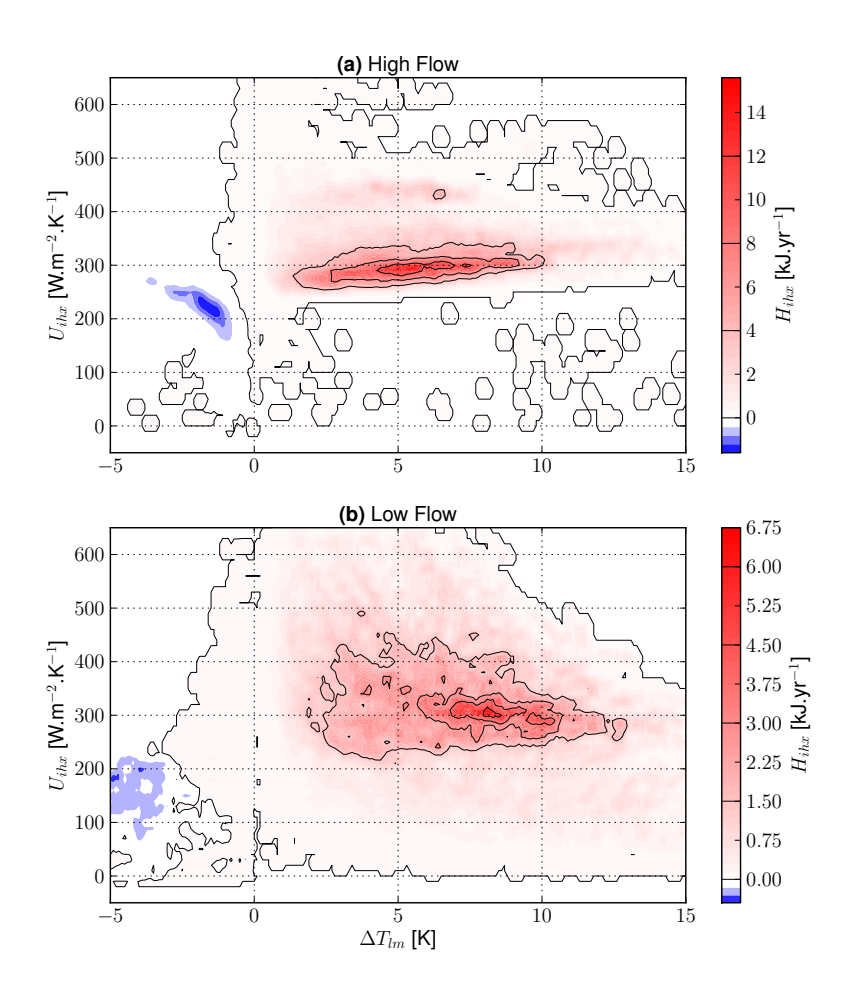


Figure 3.11: Contour plot of IHX C overall heat transfer coefficient U against the log mean temperature difference  $\Delta T_{lm}$  as output from Type 60 modelling.

#### 3.7 Calorimetry

Although there are simple ways of determining overall heat transfer coefficients, the theory in Section 2 allows us to be quite particular in determining the outside convection coefficient  $h_o$  of varying IHX geometries (Table B.1) within the experimental limitations we have identified. On top of the effect volumetric flow has on the overall convection conditions of an IHX (e.g. averaging the Nusselt numbers in Figure 3.5 over the length of the IHX gives 17.8 for low-flow and 19.8 for high-flow), we have the mass transfer convection effects of flow conditions inside the TES.

Accepting therefore the premise that we need to discretise the TES into more than one isotropic node to model this information, we are obliged to measure accordingly. To account for stratification in measurements we split the TES piecewise (linear) between Pt-100 $\Omega$  temperature sensors distributed over its height, as illustrated in Figure 3.12a. The storage tank itself was

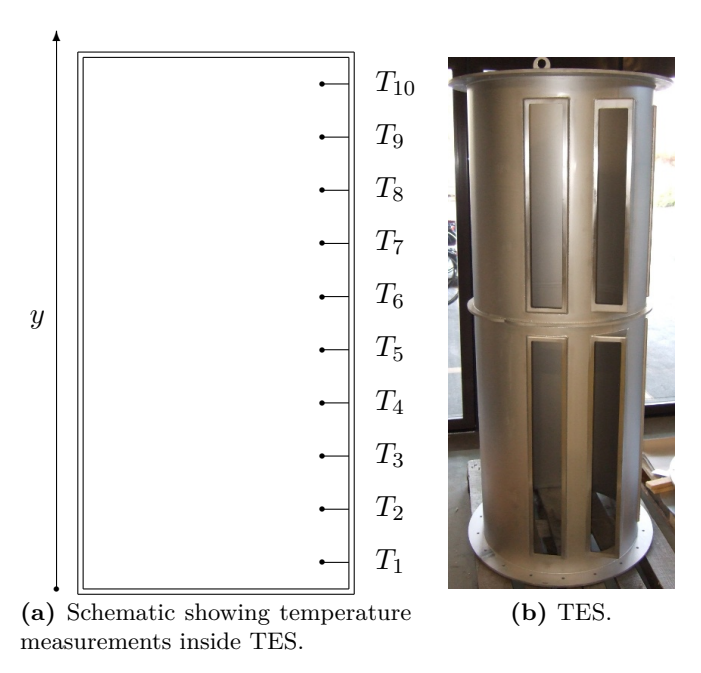


Figure 3.12: Stratification was recorded with 10 Pt-100 $\Omega$  sensors that could be interpolated piecewise over the height y.

constructed as part of a master's thesis [34] and has a diameter of 650mm and a height of 2100mm. In the case of  $400\ell$  it was only filled to a height of 1200mm. Just as the quiescent temperature of the TES was obtained, so too must the wall temperature of the IHX from inlet to outlet be measured. Figure 3.13a exemplifies how the Pt-100 $\Omega$  sensors were originally utilised to observe  $\overline{T}_w$ . Instead of linear piecewise interpolation it was discovered that a 3<sup>rd</sup>-order polynomial provided a suitable fit of  $\overline{T}_w$  to y. Unfortunately the bond conductance of this first generation of  $\overline{T}_w$  measurements was sometimes interfered with by fluid penetrating the aluminium tape and dissolving the silicone-paste; in fact the final results for IHX B had to be excluded because of this. An improvement in the Pt-100 $\Omega$  bond was achieved with soldered copper sleeves (Figure 3.13b), but only two heat exchangers could be measured thereafter.

The ideas developed in earlier sections helped define constant conditions by which the heat exchangers could be measured. Between the low and high specific collector flows of 10– $15 \ell$ .h<sup>-1</sup>.m<sup>-2</sup> and  $\geq 40 \ell$ .h<sup>-1</sup>.m<sup>-2</sup> discussed in Section 3.5, an arbitrary middle point was included and the corresponding constant flow rates of 70, 200 and 350  $\ell$ .h<sup>-1</sup>were chosen. Based on the annual simulation results from Section 3.6, constant heat transfer charging rates of 1 and 2 kW were



(a) First generation; 6 sensors mounted under aluminium tape with silicon-paste were used for IHX A, B, E, F, G and H.



(b) Second generation; 12 thermally bound (copper sleeve) sensors were used for IHX C and D.

Figure 3.13: Evolution in the accuracy and resolution of Pt-100 $\Omega$  wall temperature  $\overline{T}_w$  measurements.

also chosen. The intention in this was to keep variables constant that would otherwise have an influence on the local convection conditions while collecting data over the relevant range of temperatures we can expect. For any given set of constant charging conditions the TES was initialised at the homogeneous temperature of 20 °C and a charge continued until temperature sensor  $T_7$  in the TES - where one might expect an auxiliary controller sensor to be - reached 55 °C. The operating conditions of such a charge can be seen in Figure 3.14.

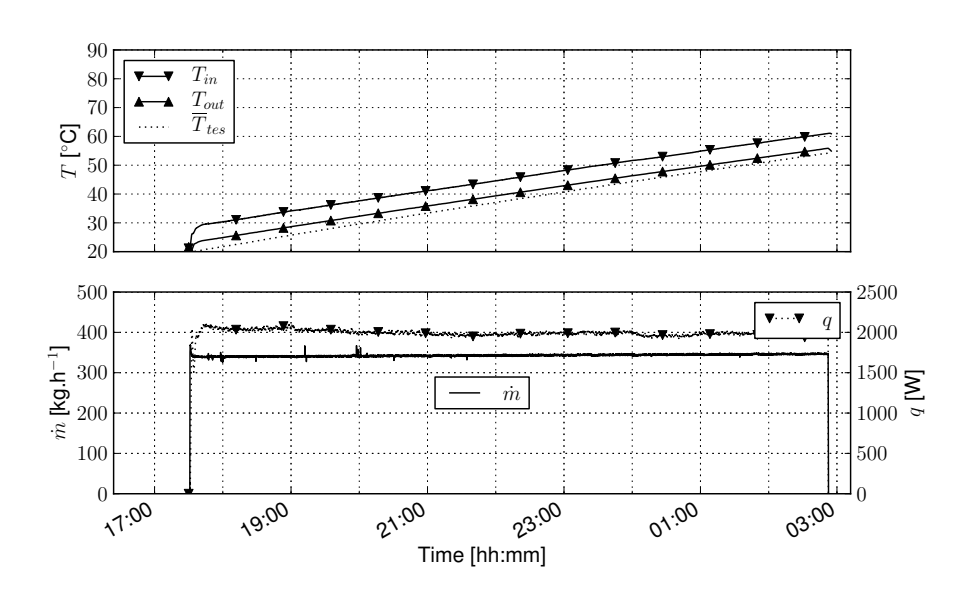


**Figure 3.14:** Plots of operating conditions of a charge with IHX C operating under 2 kW of power and a flow rate of  $350 \ \ell.h^{-1}$ .

For any point in time within a charge process we can let the iterative algorithm described in Section 2 find the convection coefficients and Nusselt numbers for the relevant temperature difference between the IHX and TES (e.g. Figure 3.15).

Averaging the experiments in time we can compare our first result in Figure 3.16 which illustrates the mismatch between Nusselt numbers from our calorimetry and those evaluated from three prominent correlations for horizontal cylinders. Although not yet mentioned, the Rayleigh

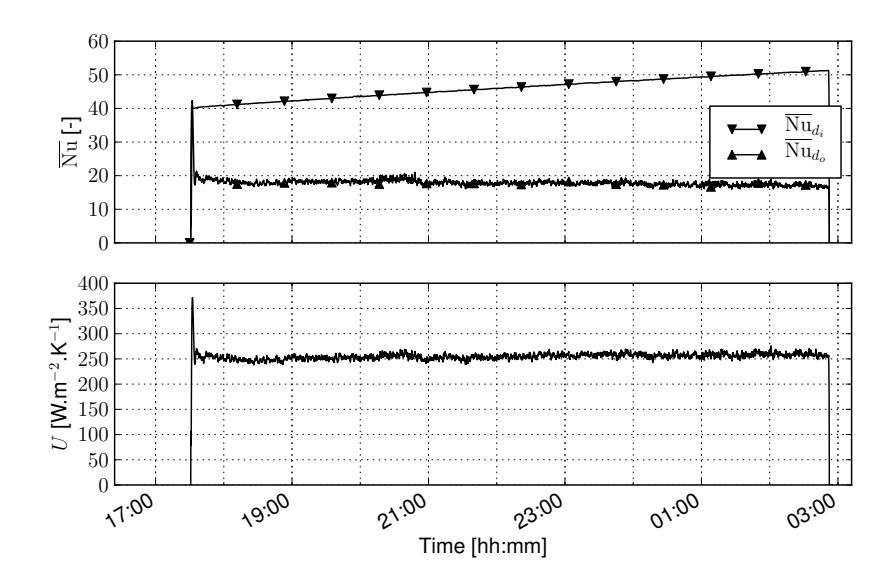


**Figure 3.15:** Plot of the calculated Nusselt numbers and overall heat transfer coefficient for IHX C operating under 2 kW of power and a flow rate of 350  $\ell$ .h<sup>-1</sup>.

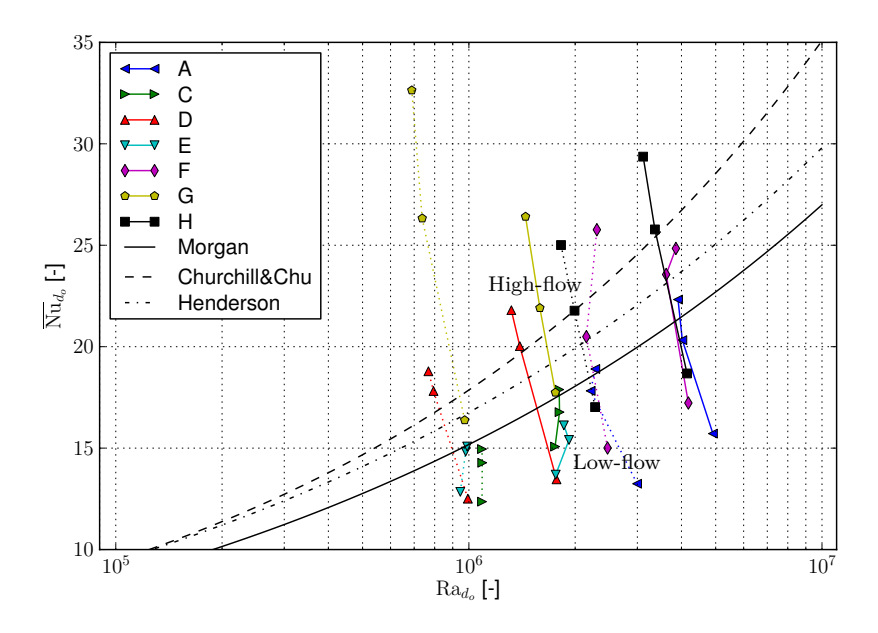


**Figure 3.16:** Results of calorimetry showing the overall Nusselt numbers plotted against their respective Rayleigh numbers; dotted lines imply 1 kW and solid lines 2 kW. For the same Rayleigh range three correlations are also shown [7, 19, 28].

number<sup>11</sup> can also be understood as an area weighted average like the Nusselt, changing over the length of an IHX in dependency of the difference between surface and quiescent temperatures. That low-flow exhibits lower average Nusselt numbers confirms what we have already noticed in Figure 3.5, that although they are high directly after the IHX inlet, they drop along the coils length quickly below that of the high-flow situation. Inversely, the Rayleigh numbers for high flow are smaller than those for low flow. In Figure 3.16 we see too how Rayleigh increases

<sup>&</sup>lt;sup>11</sup>A dimensionless parameter representing the ratio of buoyant to viscous forces:  $Ra_{d_o} = \frac{g \beta}{\nu \alpha} (T_{w_o} - T_{\infty}) d_o^3$ 

with an increase in outer tube diameter, which one would expect, seeing as the transition to turbulence is also a function of boundary layer length. It is worth noting that although we are observing Rayleigh numbers well within the laminar buoyancy regime, the correlation plotted from Churchill and Chu [7] is that indicated as being valid for the entire Rayleigh range  $(10^{-12} < \text{Ra}_{d_o} < 10^{12})$ ; this work also presented a lesser known laminar  $(\text{Ra}_{d_o} < 10^9)$  correlation that lies more or less in line with Morgan [28].

A familiarity with the Nusselt correlations for horizontal cylinders has us inquiring about their relationship to Rayleigh numbers in the simple form:

$$\overline{\mathrm{Nu}}_{d_{\alpha}} = C \, \mathrm{Ra}_{d_{\alpha}}^{n}. \tag{3.2}$$

The question of which constant C and exponent n one should use for any given IHX geometry is not clear however, for not only does the overall Nusselt number  $\overline{\text{Nu}}_{d_o}$  depend on operating conditions but also significantly on the geometry of the coil and its relation to that of the store. Laminar  $(10^{-12} < \text{Ra}_{d_o} < 10^9)$  and turbulent  $(10^9 < \text{Ra}_{d_o} < 10^{12})$  correlation functions for horizontal cylinders [28] offer values for C and n or contorted variations thereof [7]; drawing reference for example also to Prandtl numbers. Derived correlations for use with SDHW coils have thus far looked quite similar [19, 21]. We are therefore invited to explore or fit specific data as illustrated in Figure 3.17 to Equation 3.2; to be fed, for example, as inputs into Type 60 or in a simple calculation of the overall heat transfer coefficient as in Section 3.4.

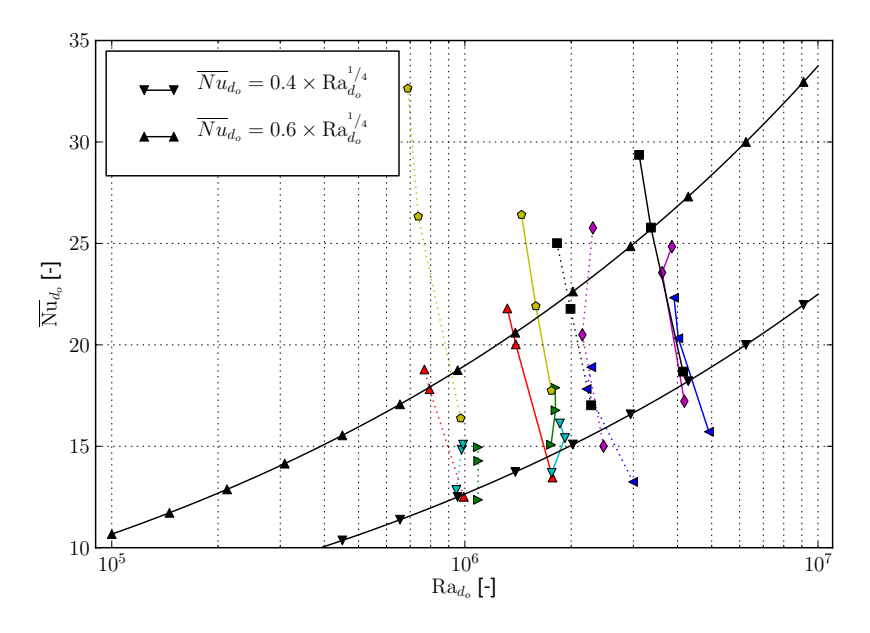
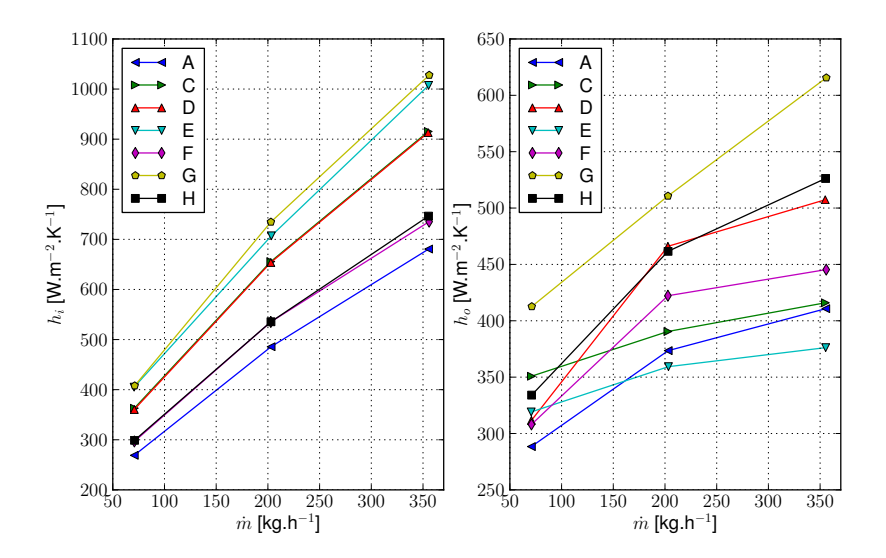


Figure 3.17: As in Figure 3.16 but with simple variations on Equation 3.2 plotted.

At this point it is worth zooming out a little to contemplate both sides of convection. In Figure 3.18 we see inner and outer convection coefficients for the 2 kW set of experiments, which is useful for gauging the relative gain in inner convection due to smaller tube diameters or the potential gain in outer convection due to geometry. Beginning with the inner convection coefficient on the left we can see the direct correlation between IHX inner tube diameter and the calculated inner convection coefficient according to [14]. In contrast the respective outer convection coefficients correlate negatively to tube diameter, and where geometry further encourages convection, for example IHX D, G and H, an additional improvement can be seen.

How these gains influence the overall heat transfer coefficient can be seen in Figure 3.19. From here we can judge with reasonable certainty<sup>12</sup> the relative performance of each IHX. The



**Figure 3.18:** Results of calorimetry showing the inner/outer heat transfer coefficients plotted against mass flow for a constant heat transfer rate  $q_{ihx}$  of 2 kW.

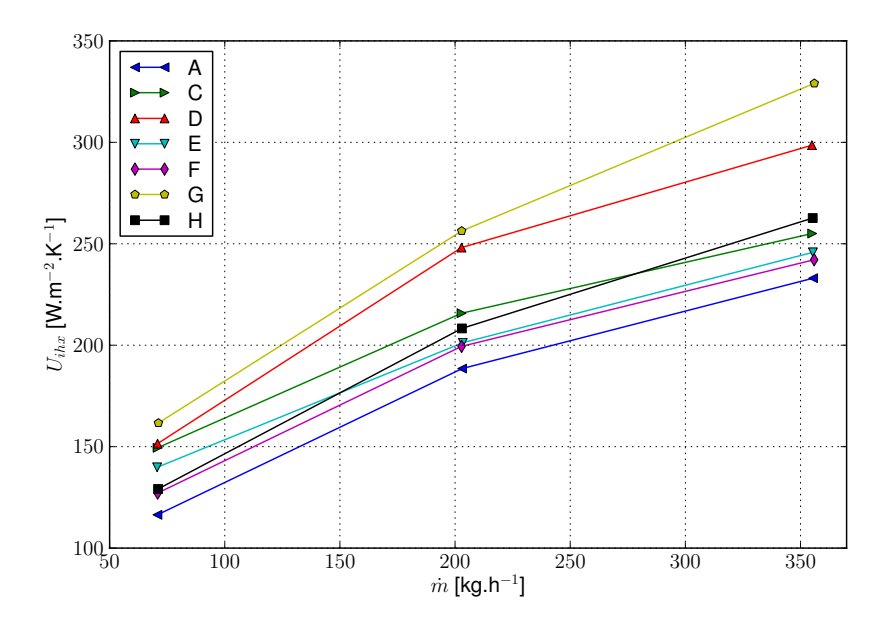
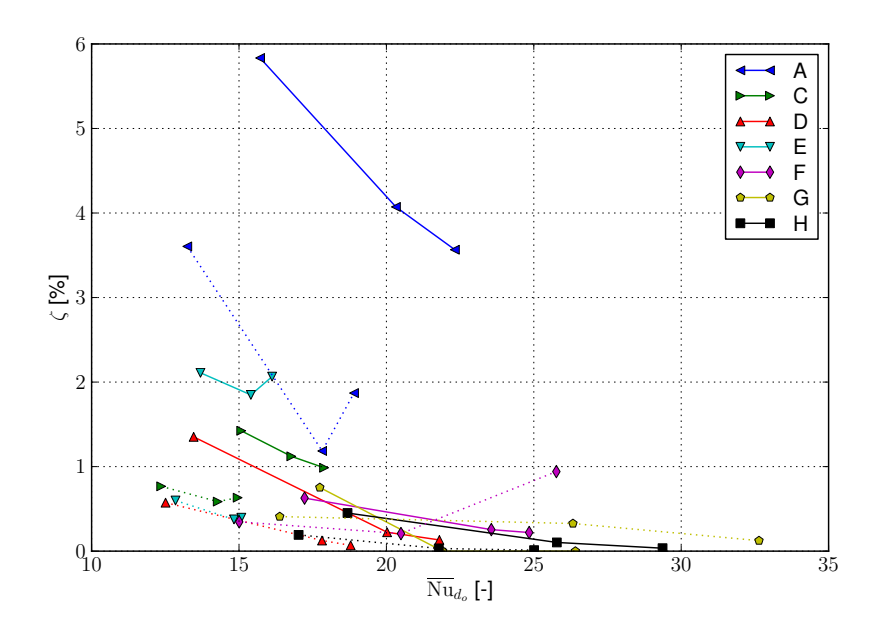


Figure 3.19: Results of calorimetry showing the overall heat transfer coefficient plotted against mass flow for a constant heat transfer rate  $q_{ihx}$  of 2 kW.

benefits of increased pitch (IHX C) and conical helix forms (IHX G and H) combined with smaller tube diameters are thus placed in perspective to those with small pitch, large tube diameters and a helix with constant radius. IHX A has the lowest overall heat transfer performance because it has the largest inner tube diameter and a small coil pitch-to-diameter ratio. IHX G and D both have small inner tube diameters and the geometry avoids having coils close and on top of one another such that plumes can diffuse the higher temperatures they contain into the surrounding quiescent fluid easier.

<sup>&</sup>lt;sup>12</sup>Remembering that wall temperature measurements for IHX A, E, F, G, and H aren't as good as for IHX C and D; experimental inaccuracy was thus estimated between 10 and 30%.

Calculating stratification efficiency ( $\zeta$ ) following the methodology from Haller et al. [17] revealed very poor values between 0 and 6% [25], when one considers that good stratification efficiencies lie in the region of 60–80%.<sup>13</sup> The highest efficiencies are observed with IHX A which has the added advantage of height within the TES due to the bottommost bent coils. A standard IHX can only introduce heat at the IHX wall temperature  $T_w$  (not  $T_{in}$ ) and at best, a height more than half way down the TES. What is perhaps less intuitive in an analysis of these evaluated stratification efficiencies is their inverse correlation to outer Nusselt numbers (Figure 3.20). It seems that whatever an IHX can boast in outer convective heat transfer performance it must forfeit on stratification efficiency.



**Figure 3.20:** Plot of stratification efficiency versus outer Nusselt numbers; dotted lines imply 1 kW and solid lines 2 kW.

<sup>&</sup>lt;sup>13</sup>These values were calculated for a directly charged TES via a constant inlet temperature entering the top of the TES. Comparison is thus not quite fair as even an IHX that is installed at the very top of a TES can only introduce heat to the TES at its wall temperature and distributed over the height of TES it inhabits.

#### 3.8 Quantitative Flow Visualisation (QFV)

Parallel to calorimetry measurements, the visualisation techniques of Particle Imaging Velocimetry (PIV) and Laser Induced Fluorescence (LIF) were explored for acquiring an axisymmetric flow and temperature field inside the TES. For a full recount of the investigations with QFV methods the reader is referred again to [34] in which varying optical access, calibration techniques and recording methodologies are discussed for accuracy and reproducibility.

Both rely on light originating from a pulsed laser to illuminate a plane within the fluid in question. Based on previous experiences [26] a cylindrical TES allowing optical access was constructed (already seen in Figure 3.12b). The laser *sheet* enters the TES through a thin window running the height of the cylinder, creating the *xy*-plane of observation illustrated in Figure 3.21a. More or less orthogonal to the laser sheet, two CCD-cameras utilising *wide-eye* lenses look into the TES through similar windows. Both laser and cameras are mounted on a *y*-translation rack for scanning the full height of the TES (Figure 3.21). Due to the nature of





(a) Axisymmetrical plane of laser sheet.

(b) In situ TES with the laser and cameras mounted on the QFV translation system to the right.

Figure 3.21: Laboratory setup including QFV equipment.

the beast we cannot obtain a single image of the whole TES at any moment in time, rather we are obliged to scan over the height of the TES with anywhere up to 10 positions. For this reason it was decided to scan between 10 and 30 images at each location before moving to the next, such that *average* flow conditions might be obtained from time series analysis. During any calorimetry measurement a scan of the TES was repeated every 15 minutes for transient variation in the flow condition.

By far the most time consuming of the two techniques, LIF utilises the temperature dependent fluorescent properties of special dyes (e.g. rhodamine based) to determine temperature within the laser sheet. Although we managed to achieve an accuracy of  $\pm 0.5-1$  K under ideal and small scale laboratory setups, the inherent measurement error - a function of laser sheet quality, fluid homogeneity and user calibration finesse - sometimes exceeded  $\pm 5$  K in practice, especially when more than a few days lay between calibration and measurement.<sup>14</sup> The scale of temperature gradients proved to be smaller than the error of our LIF implementation and

<sup>&</sup>lt;sup>14</sup>The dyes are photo-bleached with time.

calibration over the height of the TES. This made LIF less suitable for obtaining temperature profiles than our calorimetry measurements. $^{15}$ 

In Figure 3.22 we can see two exemplary LIF images on the right hand side and a respective temperature profile extracted from it on the left. Figure 3.22a is a recording made during a charge process executed immediately after calibration and Figure 3.22b shows a recording from a charge process 2 days later. The inaccuracy of  $\pm 5$  K can be seen as being a function of the laser-sheet inhomogeneity. This is something that can be calibrated for but if a calibration is too old, photo-bleaching of the dye changes the relationship between laser light intensity and the fluorescent signal. Following the measurements series on IHX A and B, no more LIF measurements were performed.

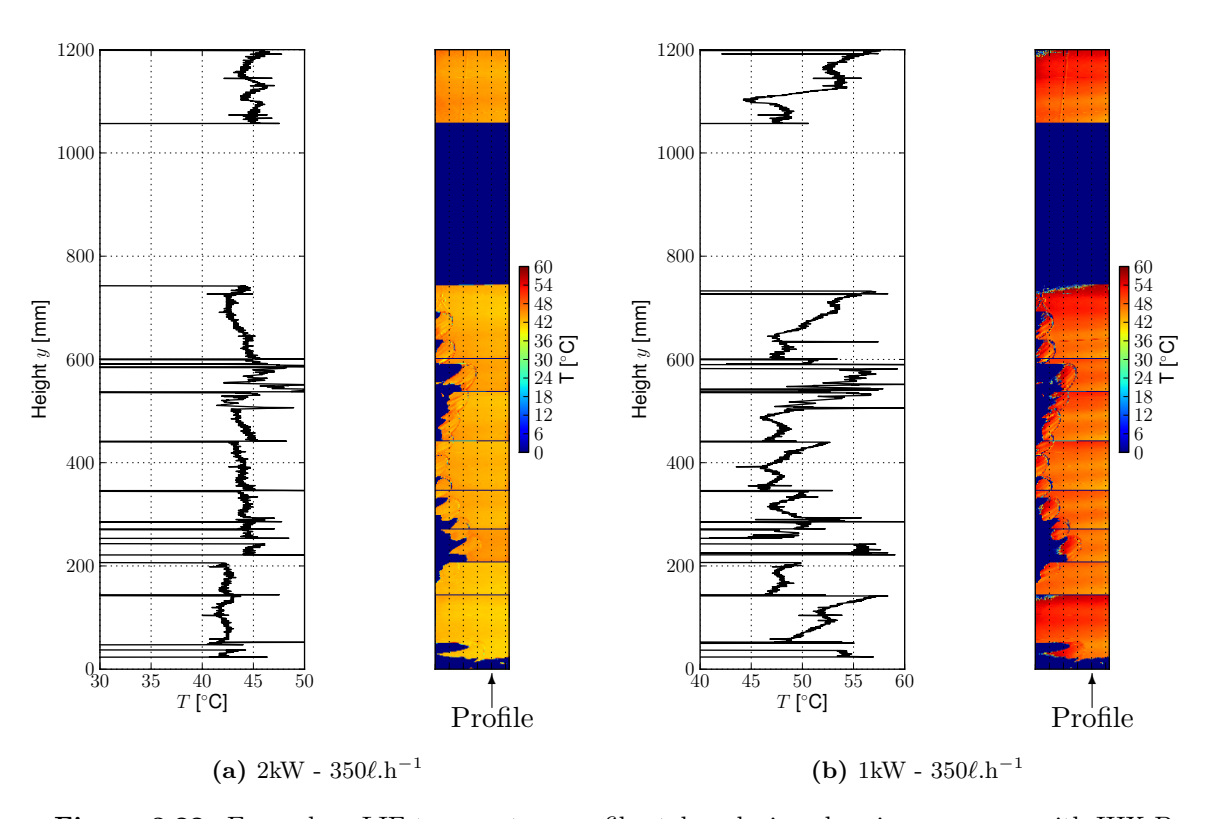


Figure 3.22: Exemplary LIF temperature profiles taken during charging processes with IHX B.

The method of PIV requires significantly more computational time for the preparation of vector images from each recorded double-image via the cross-correlation algorithm. From the immense amounts of data for each experiment<sup>16</sup> a time-series average reduced all images from a specific scan height to a single vector set. Vector interpolation then allowed for a joining of all scanned heights to one vector set. Thereby an averaged preparation of the data allows comparison with computational calculations made under the Boussinesq hypothesis (RANS<sup>17</sup>) in Section 3.9. An example of two such vector sets is shown in Figure 3.23 The first thing we notice in comparing Figures 3.23a and 3.23b is that the magnitude of flow is greater for IHX D. A closer analysis of the vectors however suggests that what we are observing in this

<sup>&</sup>lt;sup>15</sup>This does not make LIF generally unsuitable for TES observations; for example, it has been shown to deliver very good results in the study of entrainment of stratification devices [18].

 $<sup>^{16}</sup>$ For an experiment that ran up to 22 hours, upwards of 100 GB of raw image data was gathered.

<sup>&</sup>lt;sup>17</sup>Reynolds-averaged Navier-Stokes equations.

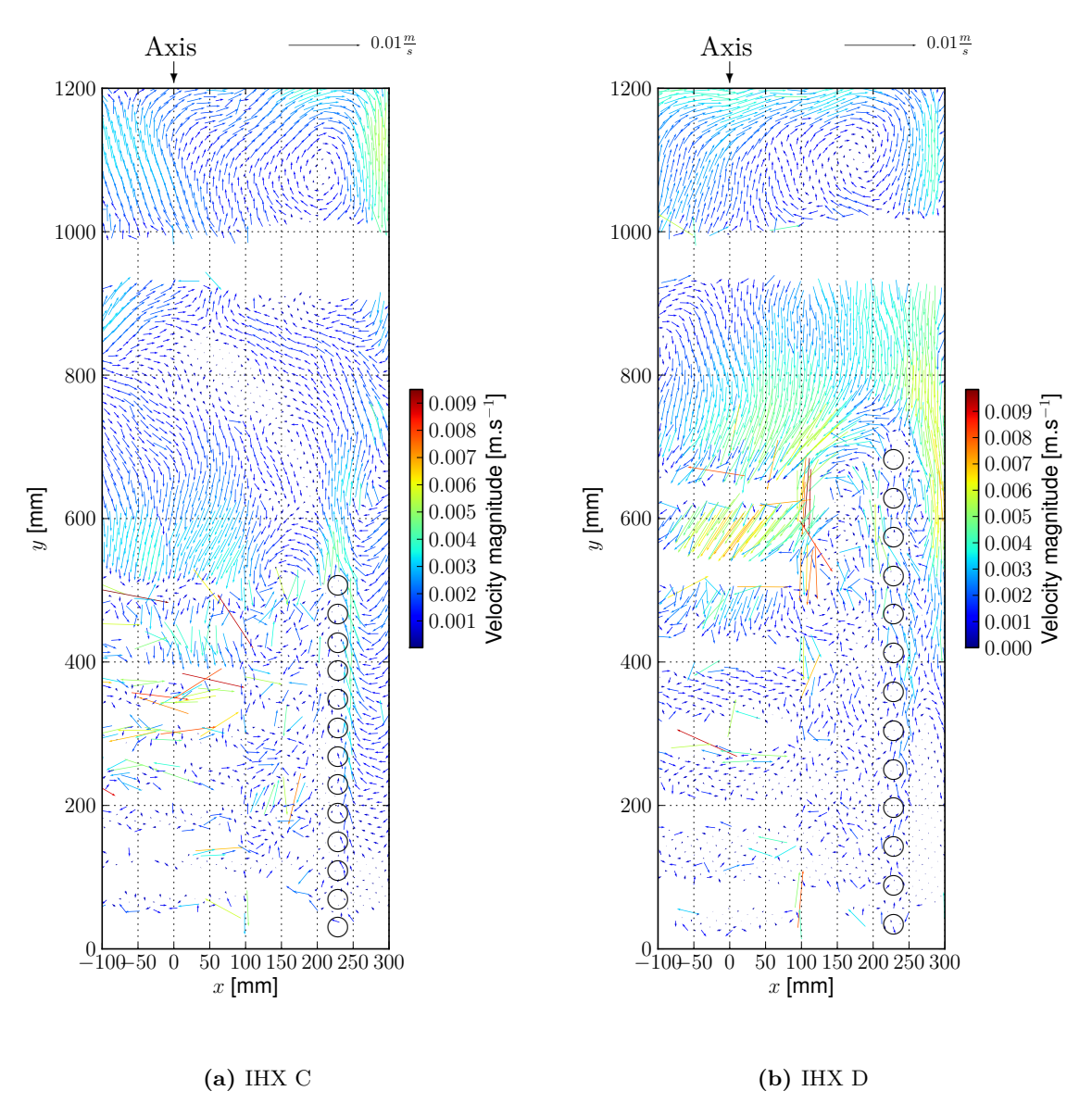


Figure 3.23: Time-series averaged PIV vector images from charging under 1kW and  $350\ell$ .h<sup>-1</sup>; the vector sets have only been partially *cleaned* of cross-correlation artefacts such that the reader can see the difference between sensible and non-sensible vectors.

axisymmetric plane is predominately a downwards flow. Unfortunately we could not capture the entire plane within the TES, otherwise we might see a predominately upwards flow on the opposite side of TES; closer to the inlet connection (where temperature is highest). Without full resolution within the TES it is hard to make quantitative judgement about mass transfer.

#### 3.9 Computational Fluid Dynamics (CFD)

With the development of the SIMPLE<sup>18</sup> algorithm in the early 1970s [30], a numerical solving of many fluid flow problems involving heat transfer became convenient and efficient [31]. During the 1980s and 90s the discipline of CFD began to emerge within the solar research community [22, 35, 29, 37]. With the latest developments in commercial CFD packages and CPU power being as cheap as it is, engineers today are ever more encouraged to tackle problems numerically, especially those for which an adequate mathematical model can be written.

Arguably, commercial packages today offer an impressive spectrum of modelling opportunities and significantly reduce the worry a user might have about the computational methods relied upon, but they generally come with a hefty price-tag and are in-transparent to an inquisitive eye. In the hope that the underlying computational methods could be better understood, it was decided to implement the open-source software OpenFOAM®.

The first steps involved validating the parametric generation of meshes in Gmsh and simulation in a suitable solver algorithm. Seeing as the fluids we are intending to model are more or less incompressible, we are offered a suitable starting point in OpenFOAM with a solver for buoyant heat transfer under the Boussinesq hypothesis. By this method all change in density (effective kinematic density  $\rho_k$ ) is prescribed by the deviation of temperature from some reference  $T_0$  through volumetric expansion:

$$\rho_k = 1 - \beta (T - T_0). \tag{3.3}$$

First the velocity and temperature fields are solved using the hydrostatic pressure field from the previous time-step before the pressure implicit loop is called for the current one. We are also blessed by low Reynolds numbers, even when we consider heat transfer on the inside of our coil tubing, and as such suitable *low*-Re turbulence models [32] await implementation for the consideration of angular momentum and diffusion.<sup>19</sup>

The correlation functions we are familiar with serve as a suitable validation. A detailed description of this process can be found in [24], however the basic steps are reiterated below.

#### 3.9.1 Two-Dimensional Horizontal Cylinder

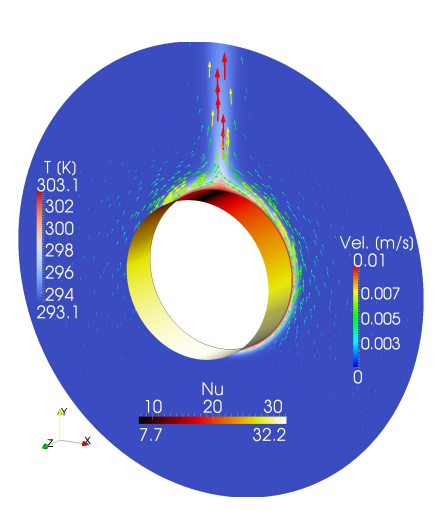
The gross simplification of our model is its reduction to two-dimensions in lieu of an *infinitely* extruded horizontal cylinder. A uniform Derichlet boundary condition is applied for the temperature of the cylinder wall and in Section 2.2 we find the necessary tools for post-processing the transient results for heat transfer.

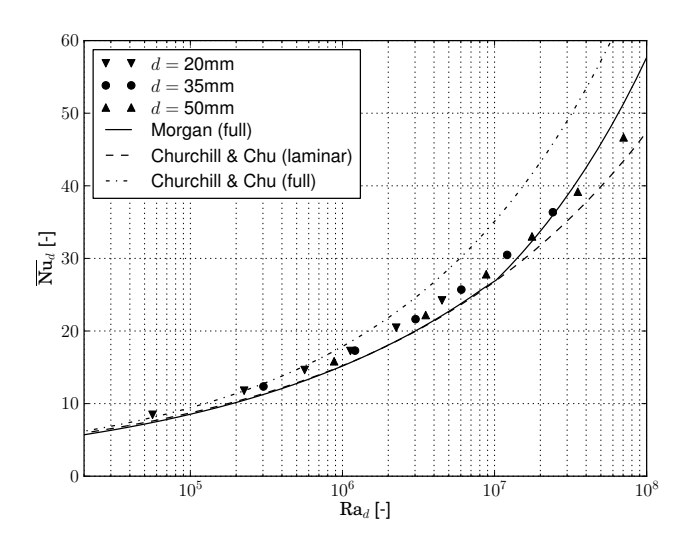
In Figure 3.24a the flow and temperature field of quiescent water at 20 °C surrounding an isothermal cylinder at 30 °C is visualised, in which we can see the variation of the cylinders Nu around its average  $\overline{\text{Nu}}_d$  of 25.6. The combined results for 3 cylinder diameters simulated under a range of temperature differences is presented with curves from correlation functions in Figure 3.24b. It is also enlightening to lose oneself in the information in Figure 3.24a; to see something one had to this point at most imagined.

Interpreting these results as a *validation* of the solver for laminar heat transfer around cylinders in general would be a little overzealous. Indeed, for our range of Rayleigh numbers and implementation under these ideal conditions, we seem to have found an agreement with reality. Not to be forgotten is that under the Boussinesq hypothesis density and viscosity are modelled independent of temperature (contant), such that the hypothesis loses accuracy as the absolute temperature rise or their differences increases. But we may cautiously press forward:

<sup>&</sup>lt;sup>18</sup>An acronym for Semi-Implicit Method for Pressure Linked Equations; this algorithm forms the basis of many CFD packages.

<sup>&</sup>lt;sup>19</sup>http://www.openfoam.com/features/RAS.php





- (a) Temperature, flow field and surface Nusselt numbers of a cylinder where d = 35mm and  $T_w = 30$ °C.
- (b) Average overall Nusselt numbers against Rayleigh numbers for 3 cylinder diameters; each simulated with 5 temperature differences ( $0.5 \le \Delta T \le 40$  K).

**Figure 3.24:** Validation of OpenFOAM to experimental correlations for horizontal cylinders in quiescent water [28, 7].

into that third dimension, multiple regions, interaction between fluids and solids and risk some unstructured discretisation.  $^{20}$ 

#### 3.9.2 Three-Dimensional Multi-Region Model

Although the trickiest and largest of models to prepare, it requires by far the simplest and most realistic boundary condition implementation. Starting with the domain at 20°C, all that is needed is a Derichlet velocity and temperature condition on the IHX inlet patch. In contrast to the definition of quiescent temperature in Section 3.9.1 as being constant, here the quiescent temperature depends on the rise in enthalpy within the store. Therefore we have to be more specific as to the definition of  $T_{\infty}$  in Equation 2.14; for example free stream temperature normal or a little to the side of the surface in question. In Figure 3.25 the results from a simulation with  $3.36 \times 10^6$  cells are shown at its  $100^{\rm th}$  second, which  $4 \times 2.66 {\rm GHz}$  processors needed 2.83 weeks to simulate. The front half of the TES volume shows Nu on the external surface of the IHX while the back half shows temperature. If one looks closely, one can see that the initialised 40 °C fluid packet from the inlet patch has just started its pass of the third and final coil, eliciting abnormally high looking Nu numbers on account of the initially very steep temperature gradient (yellow to white) occurring before conduction has warmed the quiescent fluid and convection begins.

Out of curiosity and while we have access to some nodes on a High-Performance Computing (HPC) cluster at the University of Applied Sciences in Rapperswil, the same mesh and boundary conditions as shown in Figure 3.25 was run in ANSYS13 CFX on 12 nodes with a simulation time of 500 seconds; once with a small distance between IHX coils and a second time with a high distance between IHX coils. In Figure 3.26 we can see how the Nusselt numbers look in our 3D model with a more developed flow field inside the TES.

With this underdeveloped steady-state, any observations made would be provisional and we

<sup>&</sup>lt;sup>20</sup>TetGen.

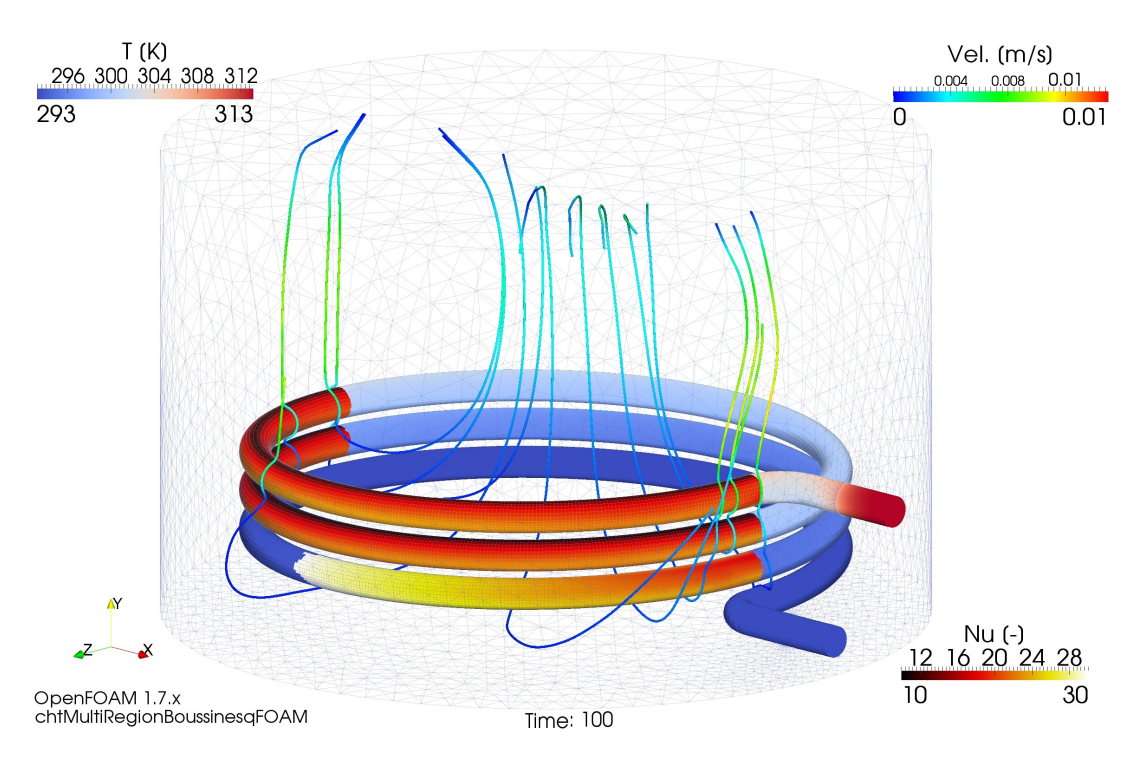


**Figure 3.25:** Exemplary IHX model simulated under the Boussinesq hypothesis with an inlet temperature of 40 °C, an initial temperature of 20 °C and an average inlet velocity of 0.033 m.s<sup>-1</sup>.

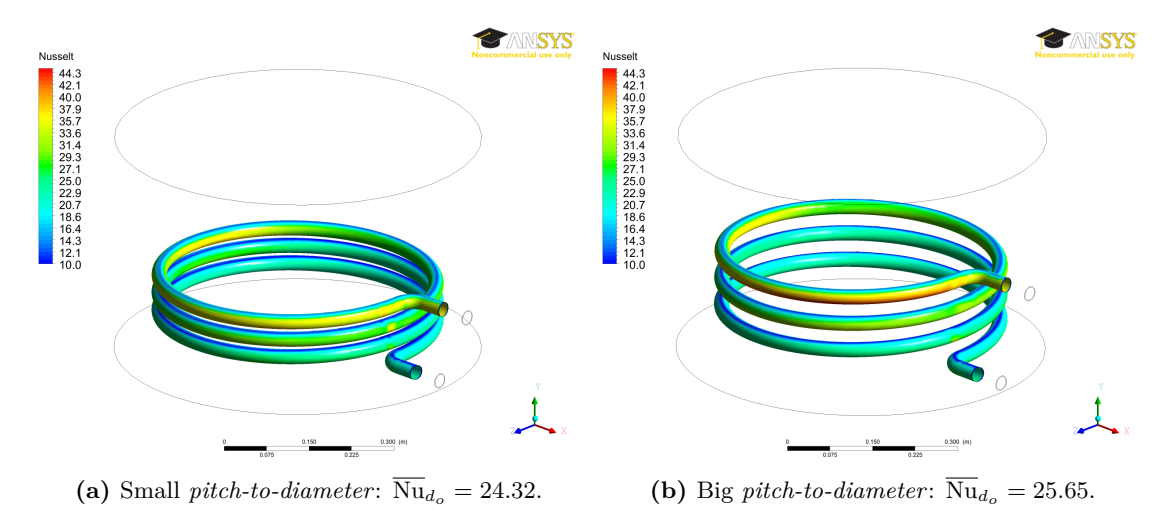


**Figure 3.26:** 3D multi-region transient simulations with ANSYS13 CFX; each simulation of 500 seconds required a little over 10 days on the HPC cluster.

are hardly patient enough to wait another 10 days before they become less so— not to mention that we haven't even modelled a full size IHX or TES yet. Faced with this dilemma one might consider a few solutions; either buy a bigger computer, rent a couple of clouds<sup>21</sup> or simplify the model somehow.

Simplification could mean a couple of things. For one we might consider reducing the resolution of discretisation by a few orders of magnitude and calibrate accordingly, perhaps implementing a *law of wall* for temperature gradients or something of the sort. Based on experience

 $<sup>^{21}\</sup>mathrm{e.g.}$  Amazon EC2® cloud computing

not delving too deep into the computational methods available [24], a reduction in the resolution of the cells around the cylinder results in an increase in Nusselt numbers evaluated, and this happens by orders of magnitude significantly smaller than ones we would have to consider. Alternatively, the mathematical modelling we looked into in Section 3.5 could be utilised to reduce the amount of independent variables (x, y, z, time) we are trying to solve for.

#### 3.9.3 Two-Dimensional Axisymmetric Model

As we reduced the problem of an infinitely extruded horizontal cylinder to 2D, so too can we reduce problems exhibiting symmetry about an axis of rotation. It does not escape our attention that we *almost* have a problem of axisymmetry; for example the temperature of the IHX coil having just entered the TES is going to be significantly higher than that which has travelled half way around the TES - an effect even more accentuated under low flow conditions.

While saving significant time in simulating with an independent variable less (z), we are obliged to model the internal flow of the IHX as a derived boundary condition. The simplest is setting either a Derichlet or Neumann boundary condition at the external tube's surface. For this, information extracted from Figure 3.5 could be used as a first estimate; either the fixed surface temperature or gradient (heat flux q'') as a function of height.

This was a fitting moment to observe a few things concerning turbulence. One of the most popular industry standard two-equation turbulence models is the so called Launder Sharma  $k - \epsilon$  model. By definition this model introduces two extra transport equations for turbulent convection and diffusion; one representing the turbulent kinetic energy (k) and the other its dissipation  $(\epsilon)$ . For our investigations we created a largely course mesh of our axisymmetric wedge inside the TES with an inflation layer resolved to within the sub-viscous layer of the IHX wall (first cell thickness  $\approx 5 \times 10^{-5}$  m).

A closer look at the Nusselt numbers during transient simulations however awoke us to a very important element of the model that we had neglected to implement properly, namely that  $\epsilon$  needs to be set to zero at the wall boundary condition when simulating under the Launder Sharma  $k-\epsilon$  model. In Figure 3.27, fluctuation of the overall Nusselt number can be correlated to

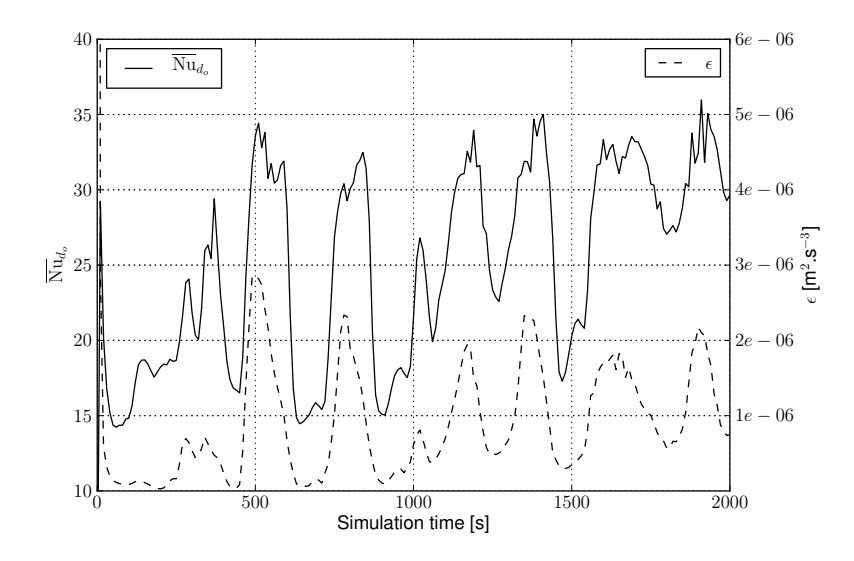
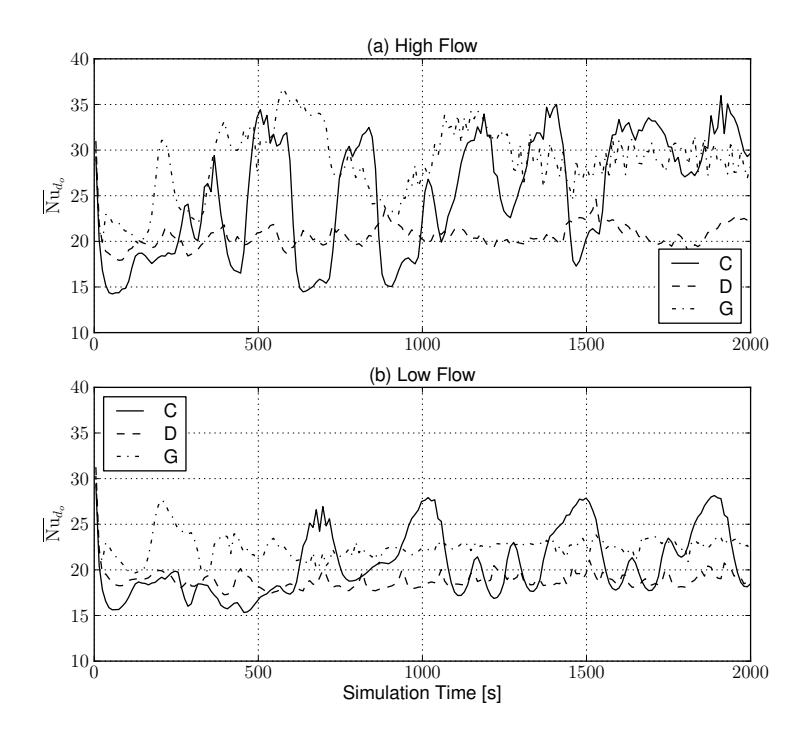


Figure 3.27: A plot of overall Nusselt number and average turbulent dissipation at IHX C's wall over a simulation time of 2000 seconds. The  $\epsilon$  boundary was implemented with a zero gradient Neumann condition.

the respective average turbulent dissipation at the IHX wall, whose every movement away from zero preceded a considerable oscillation in the overall Nusselt number. Were we to optimise using this model and Nusselt numbers as our goal function, we'd be inviting an erroneous conclusion. To illustrate this clearly, Figure 3.28 shows Nusselt numbers for IHX C, D and G over a simulation period of 2000 seconds for both high and low flow IHX wall boundary conditions. Were we to go on the law of averages in determining which IHX is better, we would find IHX C and G most encouraging options and IHX D would come out worse regardless of our modelled boundary conditions, which stands in stark contrast to that which we witnessed in calorimetry observations.



**Figure 3.28:** Transient overall Nusselt numbers for IHX C, D and G as modelled axisymmetrically under the Launder Sharma  $k - \epsilon$  model with the  $\epsilon$  boundary condition set to zero-gradient.

Changing as such the  $\epsilon$  boundary to a fixed zero condition generates Nusselt numbers much more in tune with calorimetry results, as can be viewed in Figure 3.29. More detailed simulation information can be visualised in Figure 3.30 for low flow and Figure 3.31 for high flow simulations, in particular the respective average overall Nusselt numbers are given below each sub-figure. <sup>22</sup> In the case of low flow the Nusselt numbers reflect the same performance hierarchy as we discovered in calorimetry, however in the case of high flow there is no real difference between IHX C and D, but IHX G still performs the best.

In comparison to the 3D simulations, the stagnation point on the top of every tube doesn't seem as pronounced in the axisymmetric model, which has significant implications. It seems that the angular coordinate ( $\theta$ ) dependency of Nusselt and capacitance of the tubing and fluid inside it plays a role in the stability of the external Nusselt number. The axisymmetric modelling seems a little rigid in its reaction to turbulent dissipation.

One could argue that the fixing of heat flux instead of temperature is what generated the

 $<sup>^{22}</sup>$ The axisymmetric simulations required on average between 25 and 30 hours when partitioned onto two 2.66 GHz processors.

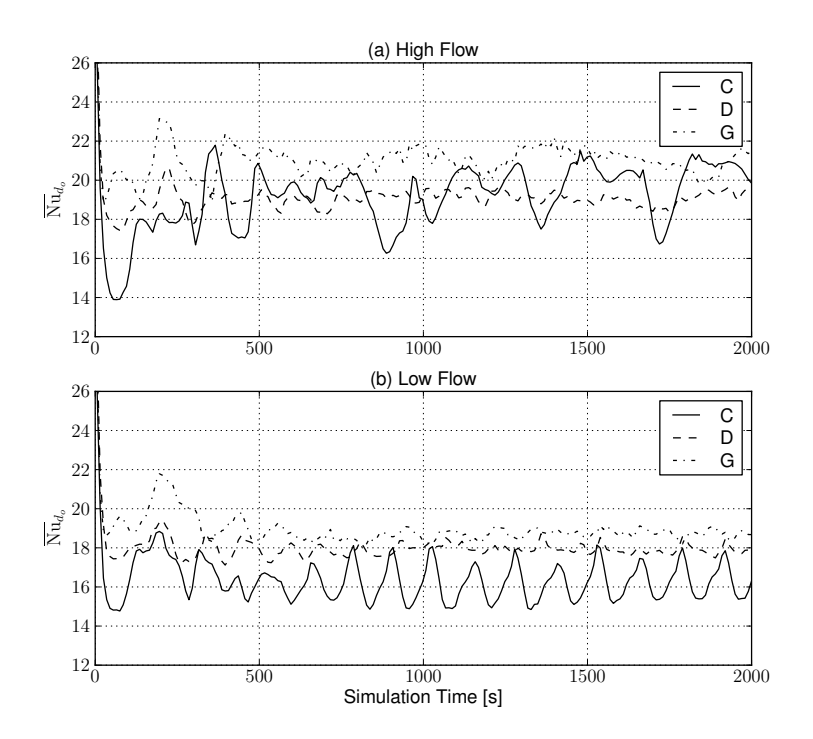
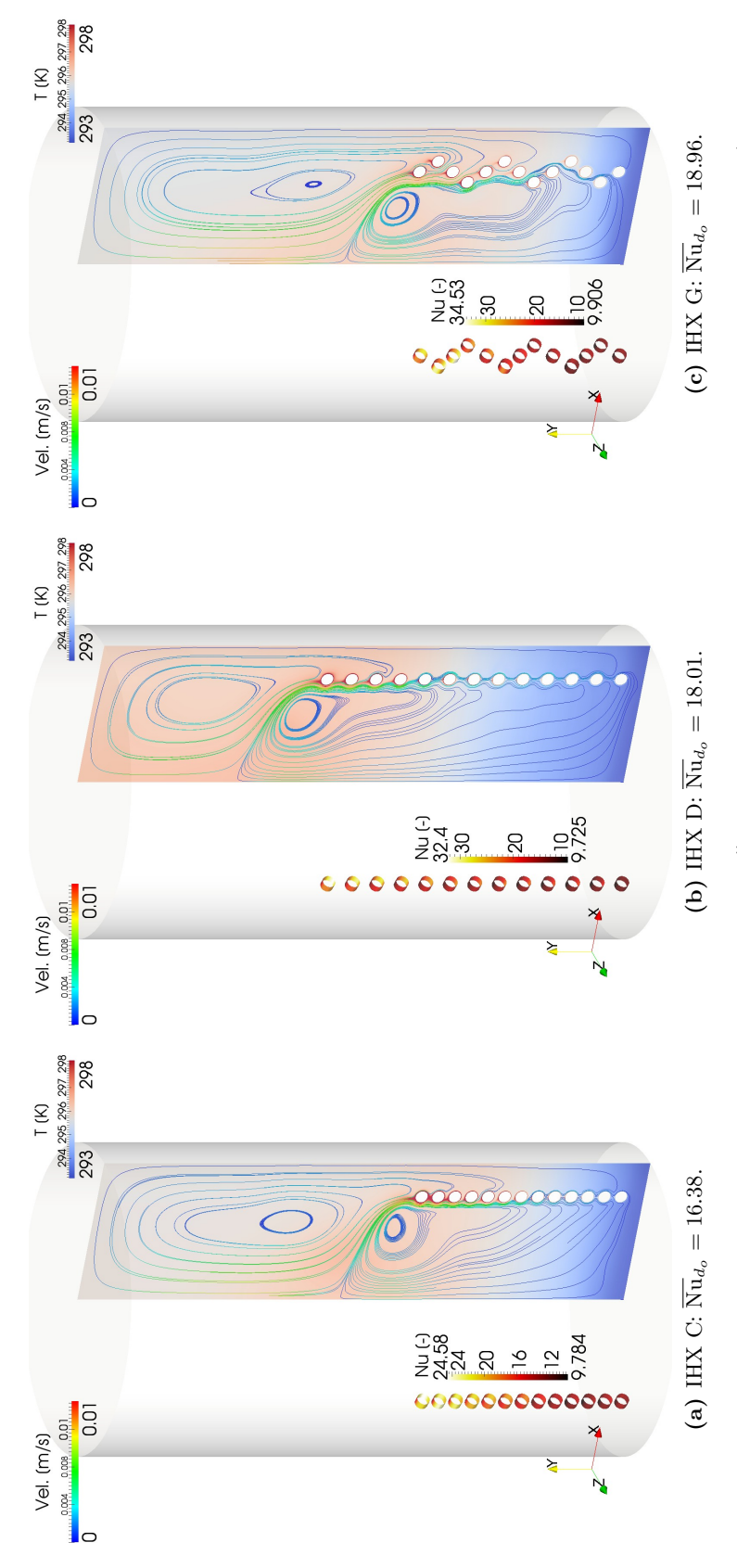


**Figure 3.29:** Transient overall Nusselt numbers for IHX C and D as modelled axisymmetrically under the Launder Sharma  $k - \epsilon$  model with the  $\epsilon$  boundary condition fixed at zero.

artefact of overzealous Nusselt numbers, but indeed a study of fixed temperature reveals the same problem. Alas, were one to use this simplified axisymmetric model for IHX heat transfer optimisation, the resulting maximum could be misleading.

If we look at the streamlines in each Figures 3.30–3.31 we can seek to commiserate the quasisteady-state mass transfer and its effect on stratification. Although a little too axisymmetric, a loose comparison of magnitude and direction to that which we have observed with PIV (Figure 3.23) reveals similar TES flow, which is qualitatively comforting. Differentiating between low and high flow and the three heat exchangers shown, we observe that the best stratification is achieved from IHX D in combination with the low flow heat flux height-profile.



The overall heat transfer rate is 2000 W and the heat flux profile reflects that of 70  $\ell$ .h<sup>-1</sup>. In each view a transfer rate is 2000 W and the heat flux profile reflects that of 70  $\ell$ .h<sup>-1</sup>. In each view a transfer rate is 2000 W and the heat flux profile reflects that of 70  $\ell$ .h<sup>-1</sup>. In each view a transfer rate is 2000 W and the heat flux profile reflects that of 70  $\ell$ .h<sup>-1</sup>. In each view a transfer rate is 2000 W and the heat flux profile reflects that of 70  $\ell$ .h<sup>-1</sup>. In each view a transfer rate is 2000 W and the heat flux profile reflects that of 70  $\ell$ .h<sup>-1</sup>. In each view a transfer rate is 2000 W and the heat flux profile reflects that of 70  $\ell$ .h<sup>-1</sup>. In each view a transfer rate is 2000 W and the heat flux profile reflects that of 70  $\ell$ .h<sup>-1</sup> is a second rate of 10  $\ell$  in the heat flux profile reflects that of 10  $\ell$  is a flux profile rate of 10  $\ell$  in the heat flux profile rate of 10  $\ell$  is a flux profile rate of 10  $\ell$  in the heat fl Figure 3.30: In these axisymmetric simulations the wall heat flux q'' of the IHX outer coil surface was defined as a function of height (see Section 3.5). numbers is shown whereas the temperature field reflects that from the last time-step at 2000 seconds.

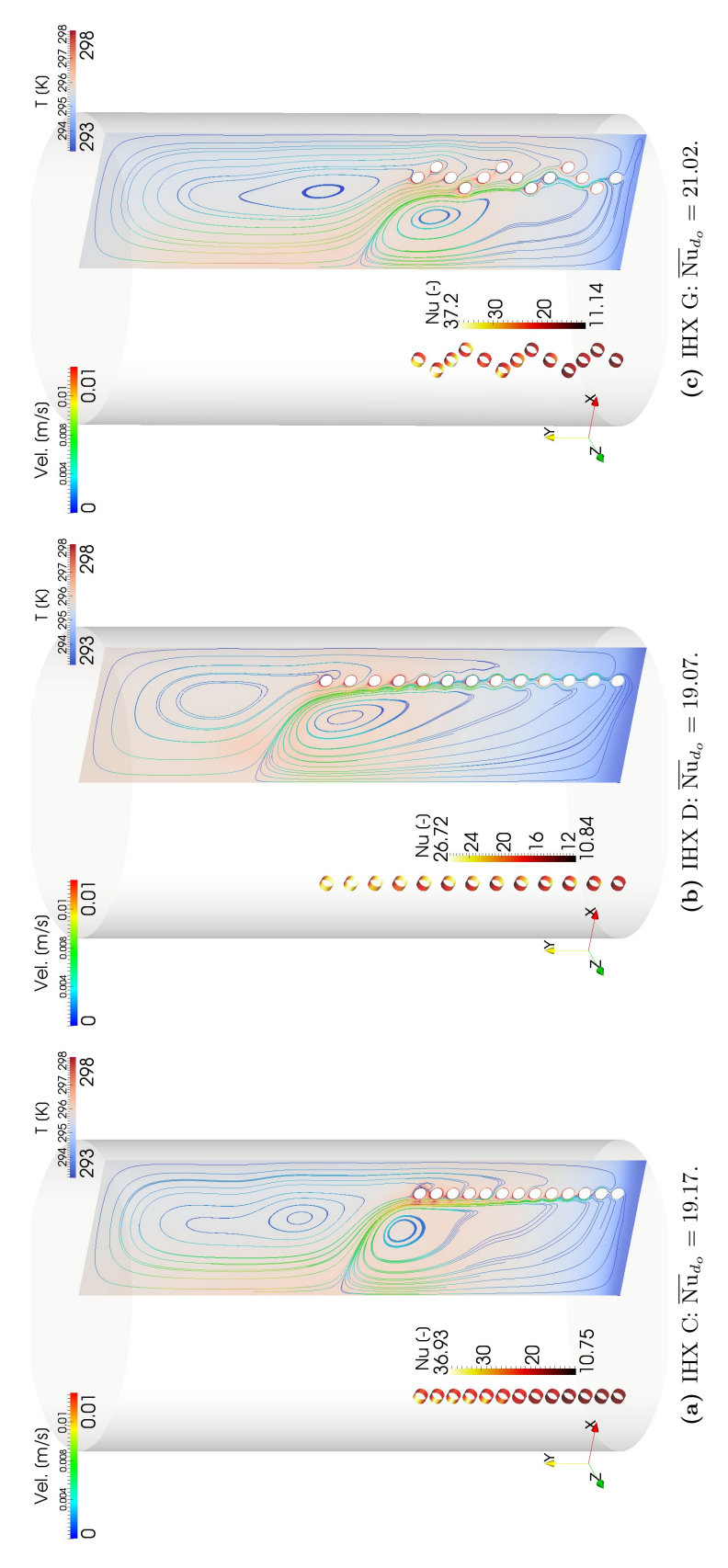


**Figure 3.31:** Axisymmetric simulations as in Figure 3.30 but where an overall heat transfer rate of 2000 W is assured via a heat flux profile reflecting that of 350  $\ell$ .h<sup>-1</sup>.

### Chapter 4

### Discussion and Conclusions

The question on our lips at the end of the day remains what shall one improve on? There is evidence in literature [36] that an improvement in heat transfer alone does not necessarily have an appreciable effect on the annual solar energy fraction of the system. An IHX itself is not known for achieving a noteworthy stratification, but rather for ensuring a robust and cheap integration of solar into the average TES design. On top of this comes the realisation that when its external convection is improved on in any way, what little potential for stratification one could speak of is further spoilt.

The most confident predictions regarding benefits in the solar design process base their assertions on annual energy savings, as derived from parameterised transient simulations. Indeed, many Norms use this in their certification procedure. What we have stressed in Section 2 is the dependency of heat transfer on geometry that has been alluded to but not fully resolved, for example TRNSYS Type 60 has the makings of modelling heat transfer with this dependency but could use some fine-tuning and adjustment; internal convection coefficient for one. Simulations parameterised from testing sequences (Type 340) have skirted this problem although the parameters themselves can seem a little cloaked.

Surprising is the difference that the higher viscosity of water-glycol in combination with coiled helixes has on the heat transfer conditions of an IHX. The detailing of these conditions in Figures 3.3–3.4 reaffirms that the very definition of high and low flow refers to the operating conditions of the collector, and not the IHX. As long as one keeps an eye on associated pressure-drop through the IHX, these authors surmise that smaller tube diameters would improve forced convection on the inside but that coil geometries should be designed with stratification in mind, and not just maximum U-values. It is possible that a generously spaced coil pitch or varying helix diameter with significantly less surface area than is standard performs better (in terms of annual solar fraction) with a higher delivery of heat via low-flow [39].

Short of resolving all the independent variables of convection as attempted in Section 3.9.2, we are obliged to accept a degree of simplification, for which the one-dimensional heat transfer model seems sufficient. Our analysis of a limited range of heat exchangers via calorimetry in Section 3.7 has bettered our awareness in its application, but due to the unforeseen complexity of the problem we did not reach our goal of finding an optimum within a full range of variables via reduced computational modelling in Section 3.9.3.

The following is a summary of our findings concerning the model variants:

• It appears that modelling external IHX convection  $\hat{a}$  la horizontal tubing is sufficiently accurate in light of experimental inaccuracies; be they laboratory, numerical or otherwise.

<sup>&</sup>lt;sup>1</sup>Higher in a twofold sense of the word; the temperature of delivery and the amount of heat delivered at the top of the IHX.

- Adjusting Nusselt number correlations according to flow-concept and geometry is sufficient in predicting the performance of an IHX until CFD modelling delivers a swifter solution.
- Although we were able to create a suitable multi-region 3D CFD model for the optimisation of IHXs, the computational time is too high for a reasonable work-flow to develop.
- The simplified axisymmetrical model decreased computational time significantly but at a cost of model accuracy. A user-defined 2D boundary condition reducing the inner wall heat flux and tube/fluid capacitance interaction might improve the axisymmetric model enough for a confident optimisation of heat transfer coefficients to become possible.

Our implementation of flow visualisation techniques was not helpful in providing quantitative answers to the questions posed. When one considers all that is currently achieved in R&D with them, the reasons for this are manifold. For example, optical access could be improved by increasing the distance of both laser and cameras to the plane of inspection, such that laser light becomes more parallel and homogeneous, and smaller objectives could be used, but this would require bigger windows and we would have lost the shape of our cylindrical TES completely. Our LIF implementation could have improved had we employed two-colour LIF<sup>2</sup>, but by that point we accepted the premise that determining Nusselt numbers with a combination of PIV and LIF is too hard a task to be achieved within the framework of this project. The authors would however recommend that any such future investigations should look into Thermography employing Thermochromatic Liquid Crystals (TLC), which is a well proven QFV technique for the examination of heat transfer from surfaces into fluids [38, 42].

<sup>&</sup>lt;sup>2</sup>Involves calibrating two fluorescent dyes; one having a temperature dependence and the other not.

### Appendix A

## Straight Tubing

For those interested, here is a simple implementation of Section 2 with functions available in EES<sup>1</sup> which was used to generate the numbers for Figures A.1 and A.2 by way of parametric tables:

```
$UnitSystem SI K Pa J
"Calculation of Immersed Heat Exchanger according to
Duffie and Beckman (2006) pp. 259-269"
"Constant Power or Temperatures? One has the option of uncommenting:
- T_in to set the inlet temperature; deactivate q and T_out,
   and keep the Nusselt function for outer horizontal cylinder activated.
 - q to set the useful heat transfer rate; deactivate T_in and T_out,
   and keep the Nusselt function for outer horizontal cylinder activated.
 - T_in and T_out; deactivate q and the outer Nusselt function Nusselt_o."
{q = -2000 [W]}
{T_{in} = 313.15 [K] "inlet"}
{T_out = 295.15 [K] "outlet"}
{m_dot = 70/3600 [kg/s]}
Fluid$ = 'Water'
P = 101300 [Pa]
                             "Pressure in pipe"
k_w = 15 [W/m.K]
                             "Conductivity of wall"
k_f = 0.6 [W/m.K]
                             "Conductivity of fluid"
c_p = 4183 [J/kg.K]
                             "Spec. heat of fluid"
RelRough = 0
                             "Relative roughness in pipe"
"Pipe diameters, radii, length and areas:"
D_i = 0.0237 [m]
r_i = D_i/2 [m]
D_o = 0.0269 [m]
r_o = D_o/2 [m]
L = 20.45 [m]
A_i = 2 * PI * r_i * L
A_o = 2 * PI * r_o * L
```

<sup>&</sup>lt;sup>1</sup>Engineering Equation Solver: don't forget to limit the iteration window by setting upper and lower limits for the variables sought.

```
"Average Temperature in storage tank:"
T_{\text{infinity}} = 303.15 \text{ [K]}
"Nusselt functions:"
"Inner:"
Call PipeFlow(Fluid$, T_f, P, m_dot, D_i, L, RelRough: &
     h_i_T, h_i_H, DELTAP, Nusselt_i, f, Re)
h_i = Nusselt_i * k_f / D_i
"Outer:"
Call FC_horizontal_cylinder(Fluid\$, T_w, T_infinity, P, D_o : &
     h_o_T, Nusselt_o, Ra)
h_o = Nusselt_o * k_f / D_o
"Overall Heat Transfer Coefficient:"
1 / (U * A_o) = ((1 / (2 * PI * r_i * L * h_i)) + &
  (LN(r_o / r_i) / (2 * PI * L * k_w)) + &
  (1 / (2 * PI * r_o * L * h_o)))
"Efficiency factor:"
F_{prime} = 1 / h_o / ((r_o / r_i) * (1 / h_i) + &
        ((r_o / k_w) * LN(r_o / r_i)) + (1 / h_o))
"Outlet temperature"
T_out = T_infinity + (T_in - T_infinity) * &
      EXP(-(h_o * A_o * F_prime) / (m_dot * c_p))
"Useful heat:"
q = m_dot * c_p * (T_out - T_in)
"Removal/Renovation factor:"
F_R = q / (A_o * h_o * (T_infinity - T_in))
"IHX flow factor"
F_dprime = F_R / F_prime
"Average wall temperature:"
T_w = T_{in} + ((q / A_o) * ((1 - F_R) / (h_o * F_R)))
"Average fluid temperature:"
T_f = T_{in} + ((q / A_o) * ((1 - F_dprime) / (h_o * F_R)))
```

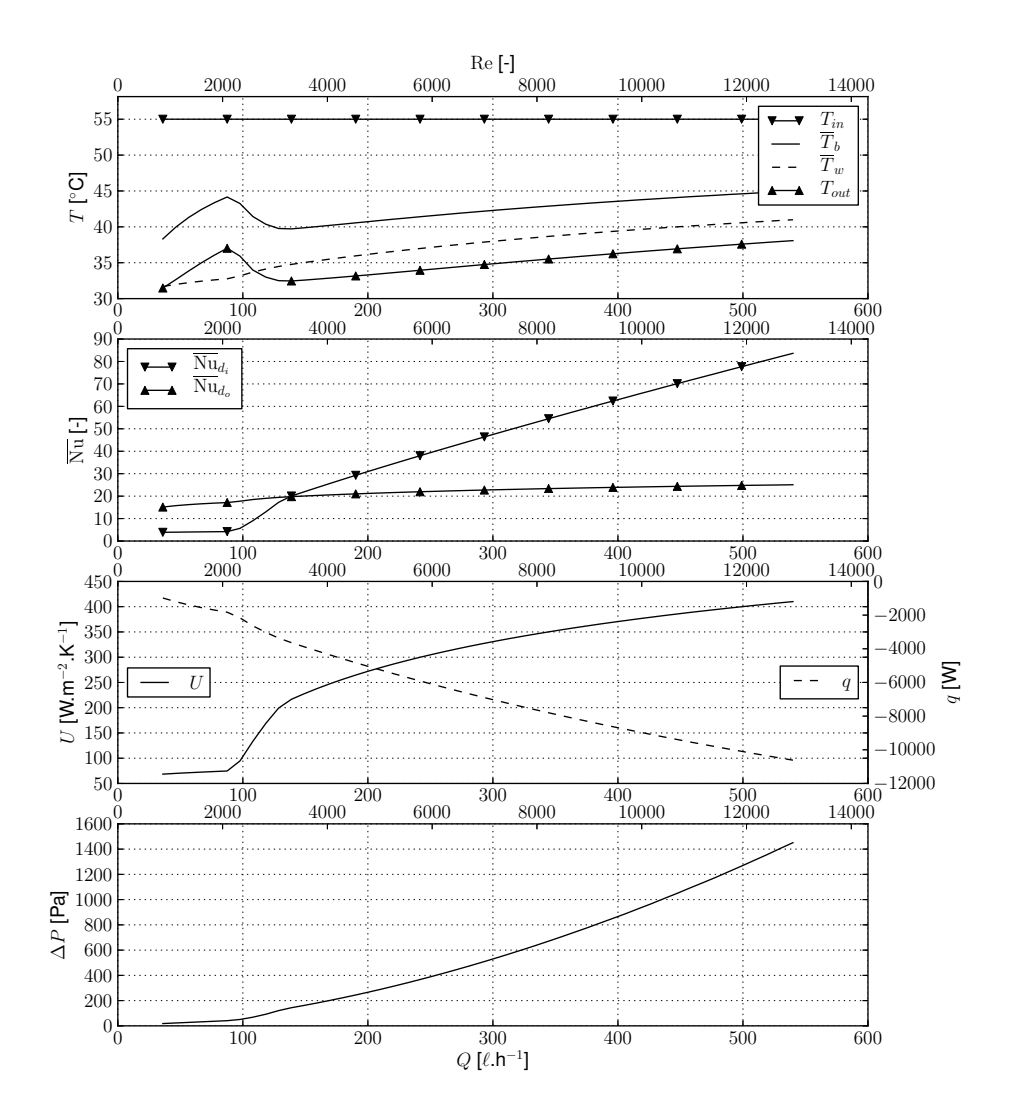


**Figure A.1:** Mass flow dependent performance of IHX C (see Table B.1) modelled in EES with a constant inlet temperature of 55 °C ( $T_{\infty}=30$  °C).

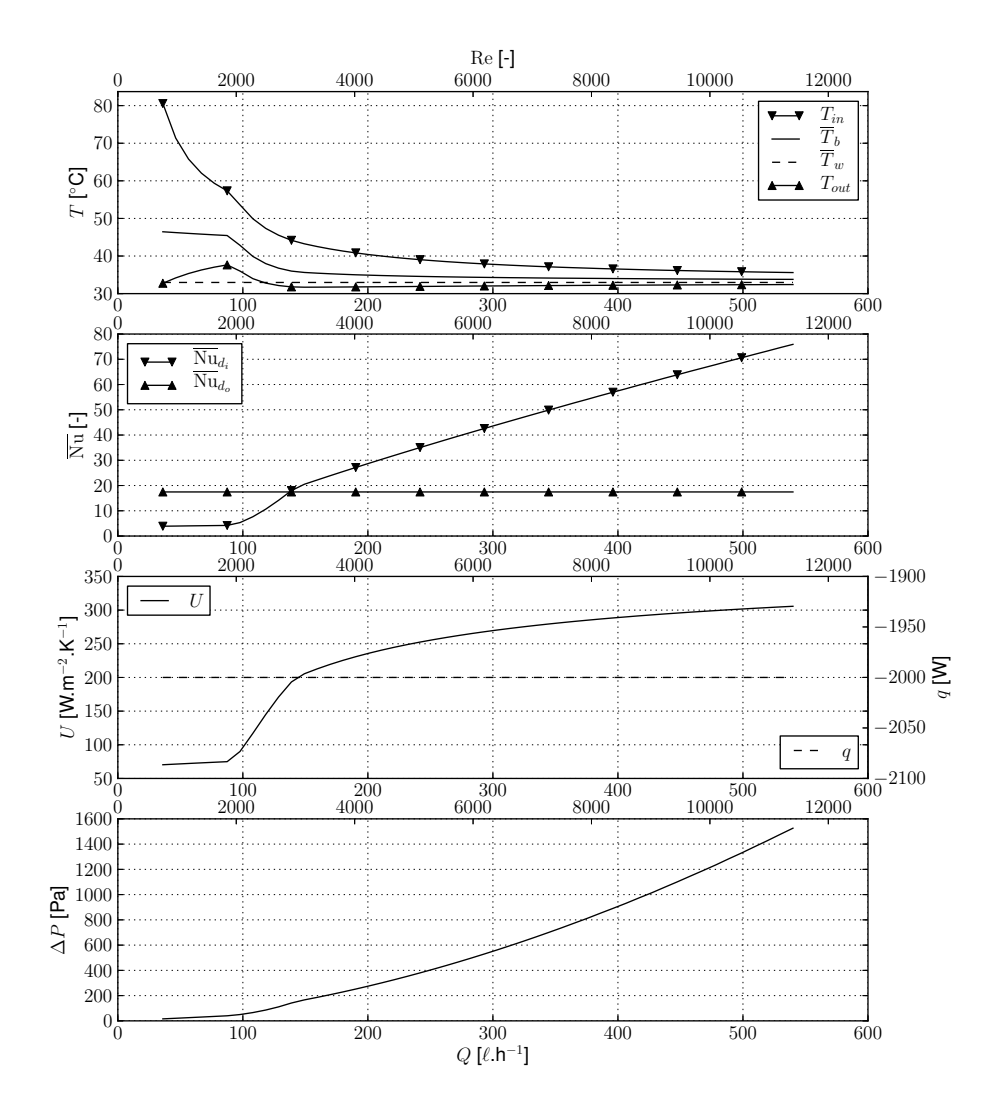


Figure A.2: Mass flow dependent performance of IHX C (see Table B.1) modelled in EES under a constant heat transfer of 2000 W ( $T_{\infty}=30$  °C).

Appendix B

Sideways Tables and Figures

**Table B.1:** Properties of the immersed coil heat exchangers tested; the acronyms ES and SS given under material specification refer to Enamelled (crude) and Stainless Steel respectively.

rude) and Stainless Steel respectively.	ess Stee	l respectively.								
			Α	В	C	О	闰	ĹΉ	ŗ	Н
Material			ES	SS	SS	SS	ES	ES	ES	ES
${\rm Conductance}  k_{ihx}  {\rm W.m^{-1}.K^{-1}}$	$k_{ihx}$	$W.m^{-1}.K^{-1}$	$\approx 40$	$\approx 15$	$\approx 15$	$\approx 15$	$\approx 40$	$\approx 40$	$\approx 40$	$\approx 40$
Inner tube $\varnothing$	$d_i$	$\times 10^{-3} \mathrm{\ m}$	30.1	28.4	23.7	23.7	21.6	27.5	21.6	27.5
Outer tube $\varnothing$	$d_o$	$\times 10^{-3} \; \mathrm{m}$	34	30	26.9	26.9	26.9	35	26.9	35
Coil $\alpha$ (avg.)	$D_{ihx}$	m	0.44	0.4	0.49	0.49	0.49	0.49	0.49	0.49
Coil height	$H_{ihx}$	m	0.75	0.62	0.475	0.7	0.47	0.46	0.46	0.46
Coil pitch	$p_{ihx}$	$\times 10^{-3} \mathrm{\ m}$	45	35	36.5	53.8	36.1	47	35	42.7
Coil length	$L_{ihx}$	m	16.63	16.9	20.45	20.63	20	15.4	16.84	14.1
Coil area	$A_{ihx}$	$\mathrm{m}^2$	1.76	1.59	1.69	1.7	1.69	1.63	1.48	1.38
								E 300		

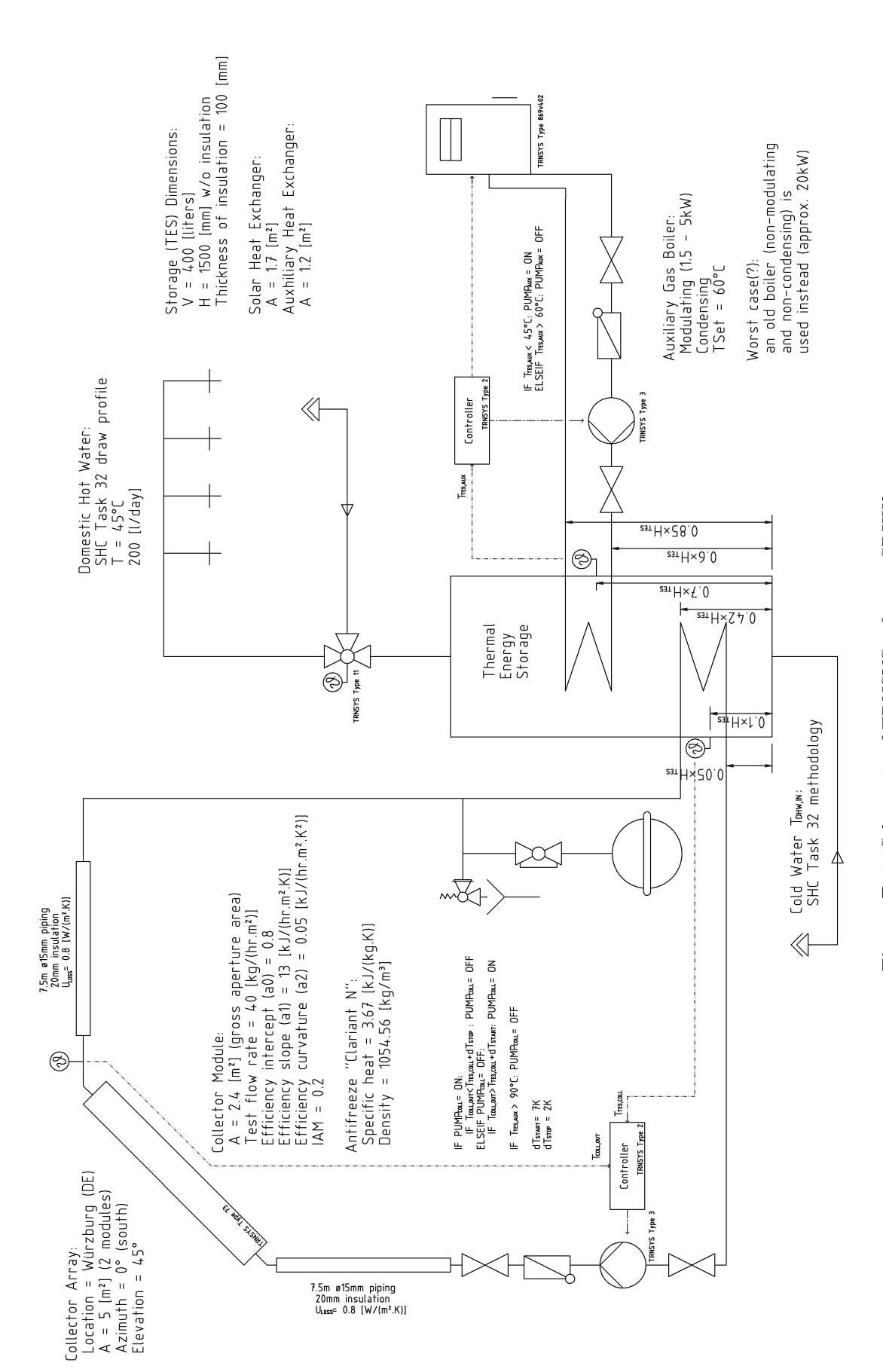


Figure B.1: Schematic of TRNSYS reference SDHW system.

# **Bibliography**

- [1] Ali, M. E. Experimental investigation of natural convection from vertical helical coiled tubes. *Int. Journal of Heat Mass Transfer* 37, 4 (1994), 665–671.
- [2] Bundesamt für Energie. Dimensionierung von Sonnenkollektoranlagen, 2001.
- [3] Cadafalch;, J. A detailed numerical model for flat plate solar thermal devices. *Solar Energy 83* (2009), 2157–2164.
- [4] CARBONELL, D., CADAFALCH, J., AND CONSUL, R. A transient model for radiant heating and cooling terminal heat exchangers applied to radiant floors and ceiling panels. In *Proceedings of ISES Solar World Congress* (Kassel, Germany, 2011).
- [5] CEN/TS 12977-2. Thermal solar systems and components custom built systems part 2: Test methods for solar water heaters and combistores, May 2008. CEN.
- [6] Chagny, C., Castelain, C., and Peerhossaini, H. Chaotic heat transfer for heat exchanger design and comparison with a regular regime for a large range of reynolds numbers. Journal of Applied Thermal Engineering 20 (2000), 1615–1648.
- [7] CHURCHILL, S. W., AND CHU, H. H. S. Correlating equations for laminar and turbulent free convection from a horizontal cylinder. *Int. Journal of Heat and Mass Transfer 18* (1975), 1049–1053.
- [8] Deutsche Gesellschaft für Sonnenergie. Solarthermische Anlagen Dimensionierung von Anlagen zur Warmwasserbereitung, 2004.
- [9] DRÜCK, H. MULTIPORT Store Model for TRNSYS, 1.99f ed. Institut für Thermodynamik und Wärmetechnik, Universität Stuttgart, Pfaffenwaldring 6, 70550 Stuttgart, Germany, March 2006.
- [10] DRÜCK, H. Mathematische Modellierung und experimentelle Prüfung von Warmwasserspeichern für Solaranlagen. PhD thesis, Uni Stuttgart Institut für Thermodynamik und Wärmetechnik, 2007.
- [11] DRÜCK, H., BACHMANN, S., AND MÜLLER-STEINHAGEN, H. Testing of solar hot water stores by means of up- and down-scaling algorithms. In *Proceedings of ISES EuroSun* (Glasgow, UK, 2006).
- [12] Duffie, J. A., and Beckman, W. A. Solar Engineering of Thermal Processes, 3rd ed. John Wiley & Sons, 2006.
- [13] EICHHORN, R., LIENHARD, J. H., AND CHEN, C. C. Natural convection from isothermal speheres and cylinders immersed in a stratified fluid. In 5th International Heat Transfer Conference (Tokyo, Japan, 1974), vol. 3, pp. 10–14.

- [14] GNIELINSKI, Y. Heat transfer and pressure drop in helically coiled tubes. In Proceedings of the 8<sup>th</sup> International Heat Transfer Conference (San Francisco USA, 1986), vol. Heat Transfer 1986, pp. 2847–2854.
- [15] Hahne, E., Kübler, R., and Kallweit, J. The evaluation of thermal stratification by exergy. In *Energy Storage Systems* (1989), Kluwer Academic Publishers, pp. 465–485.
- [16] HALLER, M. Y., CRUICKSHANK, C. A., STREICHER, W., HARRISON, S. J., ANDERSEN, E., AND FURBO, S. Methods to determine stratification efficiency of thermal energy storage processes – review and theoretical comparison. *Solar Energy 83* (2009), 1847–1860.
- [17] HALLER, M. Y., YAZDANSHENAS, E., ANDERSEN, E., BALES, C., STREICHER, W., AND FURBO, S. A method to determine stratification efficiency of thermal energy storage processes independently from storage heat losses. Solar Energy 84 (2010), 997–1007.
- [18] Hampel, M. Rechnergestützte Entwicklung von Warmwasser Wärmespeichern für Solaranlagen. PhD thesis, Universität Stuttgart, May 2008.
- [19] HENDERSON, J. B., AND CAOLO, A. C. Optimization of radial finned tube heat exchangers for use in solar thermal storage systems. Tech. Rep. DOE/R1/25247-T1, Dept. of Mechanical Engineering and Applied Mechanics, Rhode Island Univ., Kingston (USA), 1983.
- [20] Incropera, F. P., Dewitt, D. P., Bergman, T. L., and Lavine, A. S. Fundamentals of Heat and Mass Transfer. John Wiley & Sons, 2006.
- [21] KLEIN, S., NEWTON, B. J., THORNTON, J. W., BRADLEY, D. E., MITCHELL, J. W., AND KUMMERT, M. TRNSYS Reference Manual: Mathematical Reference, 16.1 ed. Solar Energy Laboratory, Univ. of Wisconsin-Madison, 2006.
- [22] LIGHTSTONE, M. F., RAITHBY, G. D., AND HOLLANDS, K. G. T. Numerical simulation of the charging of liquid storage tanks: Comparison with experimental. *Journal of Solar Energy Engineering* 111 (1989), 225–230.
- [23] Logie, W., and Frank, E. Potential improvement in the design of immersed coil heat exchangers. In *Proceedings of ISES Solar World Congress* (Johannesburg, Sth. Africa, 2009).
- [24] Logie, W., and Frank, E. A computational fluid dynamics study on the accuracy of heat transfer from a horizontal cylinder into quiescent water. In *Proceedings of ISES Solar World Congress* (Kassel, Germany, 2011).
- [25] LOGIE, W., FRANK, E., HALLER, M. Y., AND ROMMEL, M. Investigation of immersed coil heat exchangers in regard to heat transfer and storage stratification. In *Proceedings of ISES EuroSun* (Graz, Austria, 2010).
- [26] LOGIE, W., FRANK, E., AND LUZZI, A. Evaluation of solar thermal storages with quantitative flow visualisation. Tech. Rep. BFE/102340/280244, Institut für Solartechnik SPF, Rapperswil, Switzerland, 2008.
- [27] MESSERSCHMID, H. Entwicklung und Validation eines numerischen Verfahrens zur Beurteilung von Trinkwasserspeichern. PhD thesis, Universtität Stuttgart, Lehrstuhl für Heiz- und Raumlufttechnik, 2002.

- [28] MORGAN, V. T. The cverall convective heat transfer from smooth circular cylinders. In *Advances in Heat Transfer* (New York, 1975), vol. 11, Academic Press Inc., pp. 199–264.
- [29] MORRISON, G. L., NASR, A., BEHNIA, M., AND ROSENGARTEN, G. Analysis of horizontal mantle heat exchangers in solar water heating systems. Solar Energy 64 (1998), 19–31.
- [30] Pantakar, S. V. Numerical Heat Transfer and Fluid Flow. Taylor & Francis, 1980.
- [31] Pantakar, S. V., Ramadhyani, S., and Sparrow, E. M. Effect of circumferentially nonuniform heating in laminar combined convection in a horizontal tube. *Journal of Heat Transfer* 100 (1978), 63.
- [32] PATEL, V. C., RODI, W., AND SCHEURER, G. Turbulence models for near-wall and low-reynolds number flows: a review. AIAA Journal 23 (1985), 1308–1319.
- [33] Prabhanjan, D. G., Rennie, T. J., and Vijaya Raghavan, G. S. Natural convection heat transfer from helical coiled tubes. *Int. Journal of Thermal Sciences* 43 (2003), 359–365.
- [34] REBER, A. Detaillierte untersuchungen zu strömung und wärmeübertragung an eingetauchten rohrwendel-wärmeübertragern. Master's thesis, HSR Hochschule für Technik Rapperswil, 2010.
- [35] Reindl, D. T., Beckman, W. A., and Mitchell, J. W. Transient natural convection in enclosures with application to solar thermal storages tanks. *Journal of Solar Energy Engineersing* 114 (1992), 175–181.
- [36] SCHEUREN, J., PUJIULA, F., AND EISENMANN, W. Comparative measurements of two identical thermal solar systems with high-flow and low-flow rates. In *Proceedings of ISES EuroSun* (Freiburg, Germany, 2004).
- [37] Shah, L. J., Morrison, G. L., and Behnia, M. Characteristics of vertical mantle heat exchangers for solar water heaters. *Solar Energy* 67 (1999), 79–91.
- [38] STASIEK, J., STASIEK, A., JEWARTOWSKI, M., AND COLLINS, M. W. Liquid crystal thermography and true-colour digital image processing. *Optics & Laser Technology 38* (2006), 243–526.
- [39] VAN BERKEL, J., VELTKAMP, W. B., AND SHAAP, A. B. Thermal behaviour of a heat exchanger coil in a stratified storage. In *Proceedings of ISES Solar World Congress* (Denver, Colorado, USA, 1991).
- [40] VAN KOPPEN, C. W. J., THOMAS, J. P. S., AND VELTKAMP, W. B. The actual benefits of thermally-stratified storage in a small and medium size solar system. In *Proceedings of ISES Solar World Congress* (Atlanta, 1979), pp. 579–580.
- [41] XIN, R. C., AND EBADIAN, M. A. Natural convection heat transfer from helicoidal pipes. Journal of Thermophysics and Heat Transfer 10, 2 (1996), 297–302.
- [42] Yang, J. S., Hong, C. H., and Choi, G. M. Heat transfer measurement using thermochromatic liquid crystals. *Current Applied Physics* 7 (2007), 413–420.